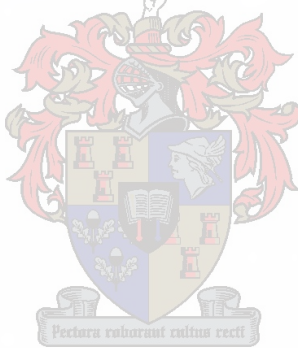


Response of NaI(Tl) detectors in geophysical applications

Nortin P. Titus



**Thesis submitted in partial fulfilment of the requirements for the degree of
Master of Science at the University of Stellenbosch**

Supervisor: Prof. A.A. Cowley

April 2005

DECLARATION

I, the undersigned, hereby declare that the work contained in this thesis is my own original work and has not previously, in its entirety or in part, been submitted at any university for a degree.

Nortin P. Titus

Date

Abstract

Airborne gamma-ray spectrometry is used for exploration and environmental monitoring over large areas. Such datasets of γ -ray are acquired using large $16l$ NaI(Tl) detector crystals mounted in an aircraft. The response of these detectors to naturally occurring radioactive isotopes is a function of detector volume, efficiency and resolution. This response is modelled using the Monte Carlo method. A photon-electron transport computer code, NIPET, is written to calculate the intrinsic efficiency and photofraction of these large prismatic crystals. The intrinsic efficiency indicates the number of incident photons that interact in some way with the detector resulting in a deposition of energy in the crystal. The photofraction, on the other hand, indicates how many of these photons that impinge on the detector are actually recorded with their full initial energy. This study presents explicitly calculated photofraction values for $16l$ NaI(Tl) crystals. Comparison of these new values, calculated with this computer program, with that of published values for small $3'' \times 3''$ crystals shows good agreement. However, for large crystals, the calculated values differ from those in the literature by almost 15%. The study also finds that for the gamma-ray energy range between 0.2 - 3.0 MeV, these detectors have an intrinsic efficiency above 90%, whereas the photofraction values range from 80% for low energy photons to above 40% for high energy photons in the case of large crystals.

Opsomming

Lug gamma-straal spektroskopie is nuttig vir eksplorasie en omgewings ondersoeke oor groot areas. Metings word tipies gedoen met $16l$ NaI(Tl) detektors wat monteer is in 'n vliegtuig. Die respons van hierdie detektors ten opsigte van natuurlike radioaktiewe isotope is 'n funksie van detektorvolume, doeltreffendheid en oplosvermoë. Hierdie respons word gemodelleer deur gebruik te maak van 'n Monte Carlo tegniek. 'n Rekenaarprogram, NIPET, is geskryf om die intrinsieke doeltreffendheid en fotofraksie vir hierdie groot prismaatiese kristalle te bereken. Die intrinsieke doeltreffendheid duï die breukdeel van die invallende fotone aan wat 'n interaksie ondergaan binne die detektor kristal en sodoende energie deponeer. Die fotofraksie, daarenteen, duï die breukdeel invallende fotone aan wat absorbeer word deur die kristal met hul volle invallende energie. In hierdie tesis word eksplisiete fotofraksiewaardes vir $16l$ NaI(Tl) kristale bereken. Goeie ooreenstemming word gevind tussen fotofraksie waardes bereken met hierdie program en die waardes gepubliseer in die literatuur vir klein $3'' \times 3''$ kristalle. Vir groter kristalle is daar egter swakker ooreenstemming. Berekende fotofraksie waardes verskil met 15% van die waardes in die literatuur. Daar word ook bevind dat vir gamma-energië tussen 0.2 - 3.0 MeV, die intrinsieke doeltreffendheid vir hierdie tipe detektors bo 90% is en dat fotofraksiewaardes wissel tussen 80% vir lae energië tot bo 40% vir hoë foton energië.

Acknowledgments

Thanks and praise to my Heavenly Father for His ever-present grace and mercy.

- I want to thank Prof. AA Cowley for his continued leadership, support and advice. In addition I thank the nuclear physics group for positive criticism and suggestions.
- This work would not have been possible without the financial support of the National Research Foundation (NRF, South Africa). Also I want to thank the Germany Embassy in Namibia for their sponsorship of a computer and GPX of Namibia and the Geological Survey of Namibia particularly the Geophysics Division for providing recorded geophysical data.
- I want to thank my close and extended family and friends for their prayers, motivation, encouragement and financial support. Without your continued commitment, I would not have been this privileged.
- Finally, Harriet Louis. Thank you for believing in me, supporting my vision and continually wanting to be there for me when I was in need and actually being there.

DEDICATION

This thesis is dedicated to my last remaining 85 year old grandmother and friend, Mrs. Cornelia Titus. Your early morning prayers and petitions for me to our Lord and Saviour, Jesus Christ, have been answered with abundant blessings, protection and guidance. Thank you Ouma-mama.

Contents

1	Introduction	1
1.1	Radiation in the Environment	1
1.2	Radiation Detection Crystals	2
1.3	Radiation Transport Modelling & Simulation	3
1.4	Thesis Structure	5
2	Gamma-ray Spectroscopy	7
2.1	Radiation Terms and Definitions	7
2.1.1	Radioactive Decay	7
2.1.2	Radiation Fields	8
2.1.3	Radiation Units	9
2.2	Gamma-ray Sources	9
2.2.1	Radioactive decay	10
2.2.2	Annihilation Radiation	13
2.2.3	Bremsstrahlung	13
2.3	Interactions with Matter	13
2.3.1	Interaction Cross Section	14
2.3.2	Linear Attenuation	14
2.3.3	Energy Transfer Mechanisms	15
2.4	Environmental Radioactivity	18
2.4.1	Uranium and Thorium	19

CONTENTS	viii
2.4.2 Uranium Parent-Daughter Activities	20
2.5 Airborne Gamma-ray Spectrometry	21
2.5.1 Methodology	21
2.5.2 Detector and Spectrometer	22
2.5.3 Data Processing	22
3 Monte Carlo Modelling	24
3.1 The Detector Response Function	28
3.1.1 Efficiency Calculations	29
3.1.2 Photofraction	30
3.1.3 Detector Smoothing	30
3.2 Attenuation Coefficients	30
3.3 Photon Transport	31
3.3.1 Geometrical Tracking	31
3.3.2 Pathlength	35
3.3.3 Photon Interaction	35
3.4 Electron Transport	39
3.4.1 Geometrical Tracking	40
3.4.2 Determination of Initial Coordinates and Directional Cosines	40
3.4.3 Bremsstrahlung	41
3.5 Simulation Algorithm and Flow Diagram	42
4 Results and Discussion	46
4.1 Response Function Comparisons	47
4.1.1 DOSRZnrc compared with Measurement	47

CONTENTS	ix
4.1.2 NIPET compared with DOSRZnrc	49
4.1.3 Response Functions For Different Crystal Dimensions	51
4.2 Efficiencies and Photofractions	56
4.2.1 Intrinsic Efficiency	56
4.2.2 Photofraction	59
4.3 Discussion	62
4.4 Radiometrics	66
4.4.1 Airborne Spectrum	66
4.4.2 Radon Contribution	68
4.4.3 Airborne Radiation Removal Techniques	68
4.4.4 Extention to Airborne Radiation Identification	69
5 Conclusion	72
Appendix	74
A Derivations of Equations	74
A.1 Derivation of Compton Scattered Photon Energy	74
A.2 The Differential Cross Section	75
B Polynomial coefficients	76
B.1 Photoelectric absorption polynomial coefficients	76
B.2 Compton scattering polynomial coefficients	76
B.3 Pair-production absorption polynomial coefficients	77
Bibliography	78

List of Figures

1.1	Diagram of a 16l NaI(Tl) detector typically used in airborne surveys	3
2.1	(a) Parent nucleus (P) decays via β -decay to an excited state of the daughter product (D) followed by γ -ray emission. (b) Parent nucleus (P) decays via β -decay to the ground state of the daughter product (D)	10
2.2	^{60}Co decay scheme	11
2.3	^{137}Cs decay scheme	12
2.4	Photo-electric absorption	16
2.5	Compton Scattering	16
2.6	Uranium and thorium decay chains [Min97]	19
2.7	Uranium and thorium γ -ray spectral profile	20
3.1	Coordinate system and detector orientation	32
3.2	Laboratory frame and photon frame	34
3.3	Polar and azimuthal angles following Compton scattering	38
3.4	NIPET program flow diagram	44
3.5	Graphical representation of photon transport in NIPET	45
4.1	Experimental set-up and instrument specifications	47
4.2	Simulated cobalt and cesium spectra superimposed on measured spectra . .	49
4.3	Simulated (a) cesium and (b) thallium spectra	51
4.4	Crystal orientations for the airborne detector	52

LIST OF FIGURES

xi

4.5 Response function and Compton scatter contribution for crystal 2 - 0.662 MeV	52
4.6 Response function and Compton scatter contribution for crystal 2 - 2.614 MeV	53
4.7 Response function and Compton scatter contribution for crystal 4 - 0.662 MeV	53
4.8 Response function and Compton scatter contribution for crystal 2 - 2.614 MeV	54
4.9 Response functions for (a) crystal 1 and (b) crystal 4 - 2.614 MeV	54
4.10 Compton scatter contribution	55
4.11 Intrinsic efficiencies calculated from eq. 4.1	57
4.12 Photofraction plot for three crystal shapes	61
4.13 Intrinsic efficiency and photofractions for a 16l airborne detector crystal	66
4.14 Airborne spectrum before processing(a) and after processing (b).	67
4.15 Airborne spectra containing airborne radiation compared to 'clean' spectra.	68
4.16 Variation of detector photofraction	69

List of Tables

4.1	Intrinsic efficiencies in percentage (%) calculated with NIPET	58
4.2	Photofraction values for three detector dimensions calculated with NIPET	60
4.3	Photofraction values calculated with eq. 3.4 and from Monte Carlo simulation	63
4.4	Calculated photofraction values for $16l$ crystals compared with published values	64
4.5	Photofraction values of a $16l$ NaI(Tl) crystal calculated with NIPET for 13 energies	71

Chapter 1

Introduction

1.1 Radiation in the Environment

Radiometrics has been used for decades to prospect for uranium and other metals associated with naturally occurring radioactive isotopes. The use of gamma-ray spectroscopy in the environment has now been extended to cover geological mapping, environmental monitoring and the qualitative and quantitative identification of radioactive contamination zones in nuclear fall-out events [ES02, KMP91, PAPI03, YcD98].

Exploration for water, precious stones, metals, minerals, oil and gas has always been a high priority for every African government and large parts of the African continent still remains to be explored. For this purpose airborne gamma-ray spectrometry, radiometrics, is used to acquire datasets that provide detailed coverage of the natural radioelement distribution in the earth over large areas. Interpreters of these datasets can easily identify anomalies associated with possible mineral deposits, hidden fault and fracture zones as well as possible water resources.

The use of portable and large thallium-doped sodium iodide ($\text{NaI}(\text{Tl})$), thallium-doped cesium iodide ($\text{CsI}(\text{Tl})$), bismuth germanate (BGO) and hyper-pure germanium (HPGe) detectors either in-situ or in automobiles or aircraft have become common practice. In particular, the use of and improvement of airborne nuclear detection equipment and methods has attracted significant attention by the academic, scientific and engineering community in recent years [KMP91, PAPI03, YcD98]. The possibility of identifying contamination areas rapidly by means of airborne methods after a nuclear accident and, in particular, a nuclear attack has fuelled this interest [CAS01].

For Namibia and the Southern African Development Community (SADC) as a whole, airborne gamma-ray spectrometry is in its infancy. Large parts of Southern Africa have been surveyed radiometrically and data are readily available to anyone interested therein. The value of airborne gamma-ray datasets for use in spectroscopy, mineral and water exploration, agricultural planning and environmental assessment studies is becoming apparent in this region. In addition, by improving nuclear detection equipment and methods the potential impact that these surveys can have in terms of scientific and economic value is self evident.

1.2 Radiation Detection Crystals

Many different radiation detection crystals are used for mineral identification, age determination, exploration and radiation contamination for qualitative and quantitative measurements in applied and environmental physics. Normally, the selection of a suitable detector is based on the nature and character of the radiation under investigation. Although any of the above-mentioned crystals can perform radiation detection competently, HPGe and BGO crystals are often favoured in nuclear activation-, alpha track- and in-situ analysis, whereas CsI(Tl) and NaI(Tl) crystals are favourites for nuclear borehole logging, seafloor mapping and airborne gamma-ray spectrometry.

Detectors used for gamma-ray detection differ in their response to this type of radiation. The response of the crystal to radiation is a function of detector volume, efficiency and resolution. The volume directly affects the light collection in the case of scintillation crystals and in the case of semiconductor crystals the electron-ion and electron hole pairs. On the other hand, the detector efficiency and energy resolution are an inherent property of the crystal type.

For airborne gamma-ray spectrometry, where the source activity being measured is low and measurement times are short, NaI(Tl) is clearly preferable. Their high density, excellent light collection, low cost, ease of manufacture into large crystals and room temperature operation underlines their popularity for airborne surveys. Although extensive

scientific literature pertaining to the properties and response characteristics of NaI(Tl) to gamma-radiation is available for small laboratory and portable cylindrical crystals, studies for larger crystal volumes, particularly for those used for airborne surveys, is comparatively lacking.

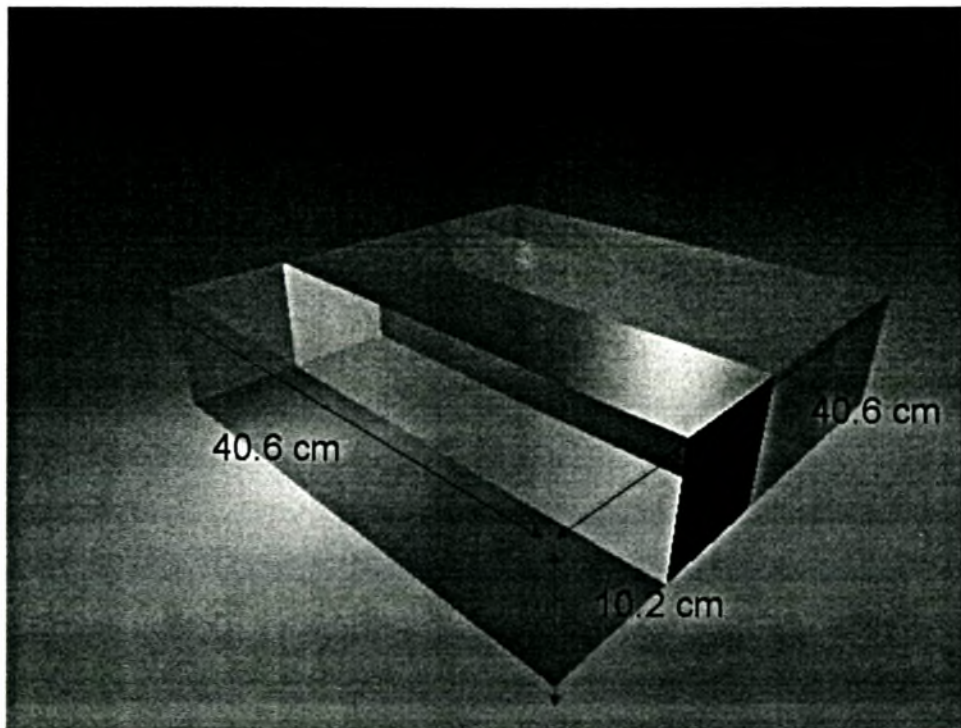


Figure 1.1: Diagram of a 16l NaI(Tl) detector typically used in airborne surveys

1.3 Radiation Transport Modelling & Simulation

Computer simulations that reproduce in a flexible way any experimental physical situation have played in recent times an ever increasing role in science and engineering. With increasing computing power and memory storage, complex problems can now be simulated on a normal desktop computer. Radiation transport problems are often simulated and the calculated results have given valuable information and insight to fields such as medical physics, reactor physics, astrophysics and high-energy particle physics.

The transport of radiation particles is characterized by propagation along straight

paths between widely spaced collision points [Pro79]. When the particle collides, absorption or scattering takes place. In the former case the incident particle is captured, whereas in the case of scattering, the particle's flight direction and energy are altered.

The Monte Carlo method simulates this radiation transport behaviour by tracking thousands of individual particles. The method is stochastic or random in nature and the results produced are statistical estimates. This method of calculation is particularly suited to radiation transport problems because the dimensions of both sources and detectors can be taken into account and modelled.

Mathematical and physical models used to approximate the migration of radioactive material in the earth, atmosphere, fluids and different solid state media are continually improved and applied in numerical calculations and computer assisted simulations. The physics describing the transport of radiation particles in a medium have been implemented in numerous Monte Carlo programs where each program addresses a specific geometrical arrangement with respect to experimental set-up, source distribution and detector composition.

For the work contained in this thesis, a Monte Carlo code, named **NIPET** (**NaI** Photon Electron Transport) is developed to compute the response function of a $16l$ rectangular NaI(Tl) crystal to mono-energetic photons in the energy range 0.1 - 3.0 MeV. Practically all of the gamma-ray photons of interest in airborne radiation surveys have energies in this range. The detector response function is computed for individual incident photon energies as well as peak and total efficiencies from which the photofraction of each energy of interest is calculated.

Other methods of modeling and simulating radiation transport are the discrete-ordinates method and the kernel method [Pro79]. The discrete-ordinates method is a numerical technique for solving the finite-difference form of the Boltzmann transport equation [Pro79]. This transport equation is based on diffusion theory where the solution of the equation gives the flux of particles into and out of a cell of interest. Other numerical and analytical techniques that solve the Boltzmann transport equation are the method of

spherical harmonics and the moments method. The kernel method treats the exponential attenuation of uncollided radiation particles originating from isotropic and parallel beam source distributions exactly and approximates the behaviour of the scattered particles by means of a buildup factor [Pro79]. The buildup factor is the ratio between the response of the detector to collided plus uncollided particles and the response from uncollided particles alone.

1.4 Thesis Structure

Following this chapter, a brief overview of the fundamental principles in gamma-ray spectroscopy is provided. The chapter begins by defining the terms and definitions used through out the thesis. Next, it looks at the origin of gamma-rays. The interaction kinematics and energy transfer mechanisms of these photons or electromagnetic waves in matter is also discussed briefly. The chapter ends with a short overview of gamma-ray spectroscopy in the environment particularly as applied to airborne gamma-ray spectrometry.

The beginning of chapter 3 outlines in further detail the objective of this study. A clear definition of the response function of a detector is given together with definitions of the peak and total efficiencies. The different features contained in this function are also described. Following this, the photon and electron transport principles used to develop NIPET are described extensively. The assumptions and approximations used in NIPET are also explained. The chapter concludes with a flow diagram of the computer code and a summary of the Monte Carlo algorithm.

Chapter 4 is divided into three parts. The first section presents the results generated by the Monte Carlo program written for this project. Firstly, detector response functions (DRFs) for two photon energies are compared to a general purpose photon-electron transport code, EGSnrc to validate the transport model derived in chapter three. Then the DRFs, intrinsic efficiency and photofraction values calculated for small and large NaI(Tl)

CHAPTER 1. INTRODUCTION

6

crystals are presented and compared to values given in the literature. The chapter ends with a look at actual recorded spectra of airborne gamma-ray surveys.

To conclude this thesis, a brief summary of the aims and objectives of this study are briefly revisited. The results are discussed in relation to this objective and recommendations pertaining to problems that arose during this study are made. Appendix A contains derivations of some equations used in this work.

Chapter 2

Gamma-ray Spectroscopy

Introduction

Gamma-ray spectroscopy is applied in many fields of science and engineering. Gamma-rays are high frequency electromagnetic waves that display a particle-like nature. The theory of their detection by radiation counters, scintillation- and semi-conductor crystals is described extensively in the literature [Att86, KN78, Kno00, Pro79].

For the purposes of this study, the origin, interaction with matter, and measurement of naturally occurring gamma radiation are discussed briefly. The theory governing the origin of gamma-rays is described as well as the interaction kinematics of gamma-rays with matter.

This chapter highlights the properties and interactions of gamma-rays and light charged particles with matter. The interaction of light charged particles becomes relevant when the energy deposited in the crystal is calculated.

2.1 Radiation Terms and Definitions

2.1.1 Radioactive Decay

The transformation of a parent particle into its daughter product is a stochastic process. However, the transformation or disintegration of a large collection of particles N per unit time is given by the decay constant λ . The decay constant is the probability per unit time that an individual particle will decay to a daughter product [Att86].

CHAPTER 2. GAMMA-RAY SPECTROSCOPY

In a closed system, the activity A in becquerel (Bq) units, is defined as the product of the decay constant and the number of particles:

$$A = \lambda N = -\frac{dN}{dt}. \quad (2.1)$$

By separating variables and integrating from $t = 0$ when $N = N_0$ to a time t , the number of particles that have not decayed is given by:

$$N = N_0 e^{-\lambda t}. \quad (2.2)$$

This is the radioactive decay law. Furthermore, the time required for half of the initial particles to disintegrate is given by the half-life, $\tau_{\frac{1}{2}}$, which is related to the decay constant by:

$$\tau_{\frac{1}{2}} = \frac{\ln 2}{\lambda}. \quad (2.3)$$

2.1.2 Radiation Fields

The *fluence* Φ is defined as the number of particles dN that enter a sphere of cross sectional area dA :

$$\Phi = \frac{dN}{dA}. \quad (2.4)$$

The *flux density* or fluence rate is the time differential of the fluence,

$$\phi = \frac{d\Phi}{dt} \quad (2.5)$$

however, in the case of a time independent field, $\phi(t)$ is constant. Then the fluence is related to the flux density by:

$$\Phi(t_0, t_1) = \int_{t_0}^{t_1} \phi(t) dt = \phi(t_1 - t_0) = \phi \cdot \Delta t. \quad (2.6)$$

In the case of mono-energetic photons with energy E_0 , the *energy fluence* Ψ is the product of the photon energy and the fluence:

$$\Psi = E_0 \cdot \Phi. \quad (2.7)$$

Similar to the flux density, the *energy flux density* is the time differential of the energy fluence, and in the special case of mono-energetic particles, the energy flux is:

$$\psi = E_0 \cdot \phi. \quad (2.8)$$

2.1.3 Radiation Units

When the radiation field interacts with matter, the *kerma* (K) describes the energy transferred to charged particles by ionizing radiation. Specifically, the kerma is the expectation value of the energy transferred to charged particles per unit mass at a point of interest, including radiative-loss energy but excluding energy passed from one charged particle to another [Att86], i.e.

$$K = \frac{d\epsilon_{tr}}{dm} \quad (2.9)$$

where $d\epsilon_{tr}$ is the energy transferred in the infinitesimal volume dV at the internal point P and dm the mass in dV . The unit for the kerma is often expressed in grays (Gy) or J/kg. For mono-energetic photons, the kerma is related to the energy fluence by:

$$K = \Psi \cdot \left(\frac{\mu_{tr}}{\rho} \right) = E_0 \cdot \Phi \left(\frac{\mu_{tr}}{\rho} \right) \quad (2.10)$$

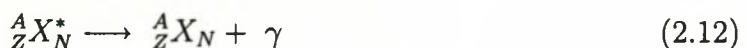
with μ_{tr} the linear energy-transfer coefficient in m^{-1} or cm^{-1} , and ρ the density of the medium in kg/m^3 or g/cm^3 .

When energy transferred to matter by all forms of radiation, whether charged or uncharged, is considered, the absorbed dose D is used to describe this energy deposition at a point P per unit mass dm , i.e.:

$$D = \frac{d\epsilon}{dm}. \quad (2.11)$$

2.2 Gamma-ray Sources

Gamma-rays are generated in the nucleus of an atom. Protons and neutrons undergo transitions from excited states to lower energy states in the nucleus of an atom and release the excess energy in the form of γ -rays. A particular nucleus will release γ -rays with well defined energies. The energy of an emitted γ -ray corresponds to the difference between the initial and the final nuclear energy level. Gamma-ray emission is described by the following reaction:



2.2.1 Radioactive decay

Radioactive decay is a principal source of gamma-rays. Nuclei decay via α , β^- , β^+ decay and electron capture. More often, gamma-rays are emitted after β -decay. We discuss gamma-ray emission following β - and α -decay in more detail.

β -decay

Beta-particles are electrons. They can be positively or negatively charged. These particles do not have discrete energies. With reference to figure 2.1, their energies correspond to

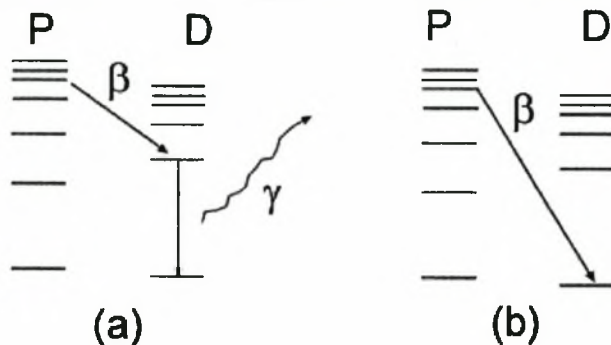


Figure 2.1: (a) Parent nucleus (P) decays via β -decay to an excited state of the daughter product (D) followed by γ -ray emission. (b) Parent nucleus (P) decays via β -decay to the ground state of the daughter product (D)

the transition energy of the parent nuclear energy state (P) to the energy state of the daughter product (D) formed. The state of the daughter product can range from an excited state (figure 2.1(a)) to the ground state (figure 2.1(b)). In the event of the parent nucleus decaying to an excited state of the daughter product, the daughter product in turn relaxes to its ground state. This nuclear relaxation process produces a γ -ray, whereby the γ -ray energy is discrete, characteristic of the difference between the nuclear energy levels. This characteristic energy allows for the unique identification of the daughter species.

As an example (see figure 2.2), Cobalt-60 (^{60}Co) decays to an excited state of nickel-60 (^{60}Ni) via β^- -decay. ^{60}Ni de-excites to an intermediate excited state releasing a 1.173

CHAPTER 2. GAMMA-RAY SPECTROSCOPY

11

MeV γ -ray and then to its ground state with release of a second 1.332 MeV γ -ray. With $\bar{\nu}$ the antineutrino, the following equation describes the nuclear reaction:

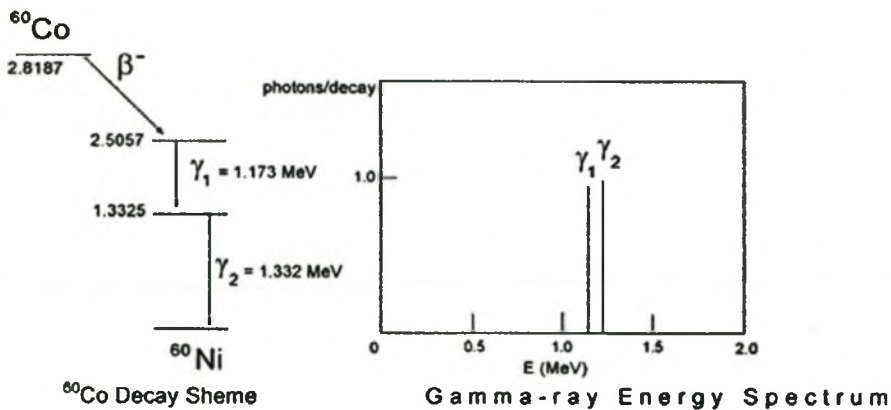
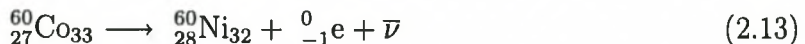
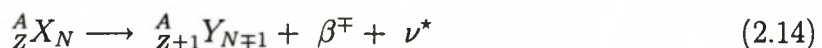


Figure 2.2: ${}^{60}\text{Co}$ decay scheme

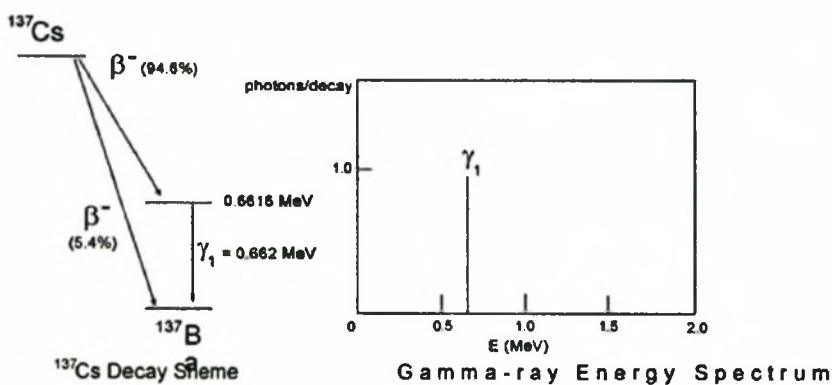
During β^- -decay, a neutron in the parent nucleus transforms to a proton. Conversely, a proton in the parent nucleus transforms to a neutron during β^+ -decay. Equation (2.14) can be written in a general form as:



where X and Y represents the parent and daughter nuclear species respectively and ν^* an antineutrino in the case of β^- -decay and a neutrino in the case of β^+ -decay.

A second example of γ -ray production is cesium-137, ${}^{137}\text{Cs}$. Cesium also decays via β^- to an excited state of barium-137; subsequently ${}^{137}\text{Ba}$ decays to its ground state with the emission of a 0.662 MeV γ -ray. However there is a 5.4% probability that ${}^{137}\text{Cs}$ will decay to the ground state of ${}^{137}\text{Ba}$ with no γ -ray emission. Accordingly, ${}^{137}\text{Cs}$ has a 0.946 probability of decaying to an excited state of ${}^{137}\text{Ba}$, and a 0.054 probability of decaying to the ground state of ${}^{137}\text{Ba}$. These probabilities are also known as branching ratios.

Beta-particles lose energy through interactions with orbital electrons of the material's

Figure 2.3: ¹³⁷Cs decay scheme

atoms and through electromagnetic radiation while slowing down in the material. Their range or travel distance in an absorber is typically in the order of a few centimeters.

α -decay

Alpha decay is common in heavy isotopes. Alpha particles are heavy, positively charged particles consisting of two protons and two neutrons. The decay process is written as:



where X and Y represents the parent and daughter nucleus respectively. The energy of an α -particle also corresponds to the transition energy of the parent nucleus to an energy state of the daughter product formed. In the event of the daughter nucleus being in an excited energy state, it will subsequently return to its ground state with the emission of a γ -ray.

Gamma-ray emission following α -decay is not as common as in β -decay, however it does occur. Energies of α -particles from natural transitions are typically between 4 - 6 MeV. Their range in materials is typically a few millimeters.

2.2.2 Annihilation Radiation

A common calibration source, Sodium-22, ^{22}Na , is a good example to illustrate γ -ray production through annihilation radiation. ^{22}Na decays to an excited state of Neon-22, ^{22}Ne , via β^+ -decay. The excited daughter nucleus relaxes to its ground state, emitting a 1.274 MeV γ -ray. The β^+ particle in turn collides with a free electron of the surrounding medium. The two particles disappear and two 0.511 MeV γ -rays are created at the location where the collision occurred. The two photons travel in opposite directions away from the collision point. This type of electromagnetic radiation is known as annihilation radiation.

2.2.3 Bremsstrahlung

Accelerated charged particles emit electromagnetic radiation. In the case of electrons, electromagnetic radiation called *bremsstrahlung* is emitted as these particles are slowed down through Coulomb interactions along their path in a medium. Bremsstrahlung energies are continuous with energies ranging from zero to the initial kinetic energy of the traveling electron.

2.3 Interactions with Matter

Gamma-rays interact with the surrounding medium mainly through collisions with atomic electrons or nuclei. Unlike charged particles, γ -rays do not have a definite range, therefore γ -rays cannot be stopped by any medium but are only *attenuated*. Gamma-ray travel paths are considered to be straight, until an interaction takes place, where upon its direction and energy are altered.

Gamma-rays within the energy range of interest, transfer their energy in a medium predominately through four mechanisms. These are *photoelectric absorption*, *coherent scattering*, *Compton scattering* and *pair production*. We consider each mechanism separately.

The probability per unit pathlength that a gamma-ray of energy E will interact with its surrounding medium and subsequently transfer energy to the medium is given by the total attenuation coefficient. The total attenuation coefficient is the sum of the attenuation coefficients for each interaction type.

2.3.1 Interaction Cross Section

The interaction cross section is the probability that a particle will undergo a particular interaction with an atom or electron in its surrounding medium. Interaction cross sections, σ , are given in barn/atom whereas the attenuation coefficients, μ , are given in cm^{-1} .

The interaction cross section for each interaction type, photo-electric absorption, Compton scattering and pair production for a particular γ -ray energy are given in nuclear data sheets. However, empirical polynomials to calculate each interaction cross section is also available [AIJ81]. Additionally, for Compton scattering, the differential cross section per scattered photon energy is given by the Klein-Nishina formula [Pro79]:

$$\frac{d\sigma}{dE} = \frac{\pi r_e^2}{mc^2} \cdot \frac{Z}{\alpha^2} \cdot \left[\eta + \frac{1}{\eta} - \frac{2}{\alpha} \left(\frac{1-\eta}{\eta} \right) + \frac{1}{\alpha^2} \left(\frac{1-\eta}{\eta} \right)^2 \right] \quad (2.16)$$

where the constants m, r_e, c and Z have their usual meaning and $\eta = E/E_0$ the ratio between the initial energy E_0 and the scattered energy E ; also $\alpha = E_0/(mc^2)$.

2.3.2 Linear Attenuation

Radiation particles N_0 incident on a material of thickness dl undergo interactions as they traverse through the medium. The change in the number of particles dN due to absorption or scattering in the medium is then:

$$-\frac{dN}{dl} = \mu N \quad (2.17)$$

Separating variables and integrating from $L = 0$ to L gives the exponential attenuation law:

$$N = N_0 e^{-\mu L} \quad (2.18)$$

where μ is the total linear attenuation coefficient. The value of N excludes the secondary particles produced during scattering.

2.3.3 Energy Transfer Mechanisms

Photoelectric Absorption

Photoelectric absorption increases with decreasing γ -ray energy. An incident γ -ray with energy E_0 collides with an atomic electron and transfers all its energy to the electron. The incident γ -ray disappears and a photo-electron is ejected from the atom. The resulting kinetic energy of the electron T_e is then the incident γ -ray energy minus the atomic binding energy E_B :

$$T_e = E_0 - E_B \quad (2.19)$$

The vacancy created is rapidly filled by an electron from the next outer shell. A characteristic X-ray with energy E_B is emitted with the transition of the outer electron to the vacant shell. The X-ray can be quickly absorbed by a loosely bound electron in an outer atomic shell. Another electron is then ejected from the atom with its vacancy quickly filled. This process is repeated a number of times. The sum of the energies of all the ejected photoelectrons will then be equal to the incident photon energy. The photo-electric absorption process is shown in figure 2.4.

Coherent Scattering

Coherent scattering or *Rayleigh scattering* is prominent for photons with energies less than 0.1 MeV. An incident γ -ray is scattered by an electron transferring virtually no energy to the electron. The γ -ray changes direction retaining practically all its energy. The atom, however, is neither excited nor ionized. In radiation measurements above 0.2 MeV, coherent scattering is normally neglected.

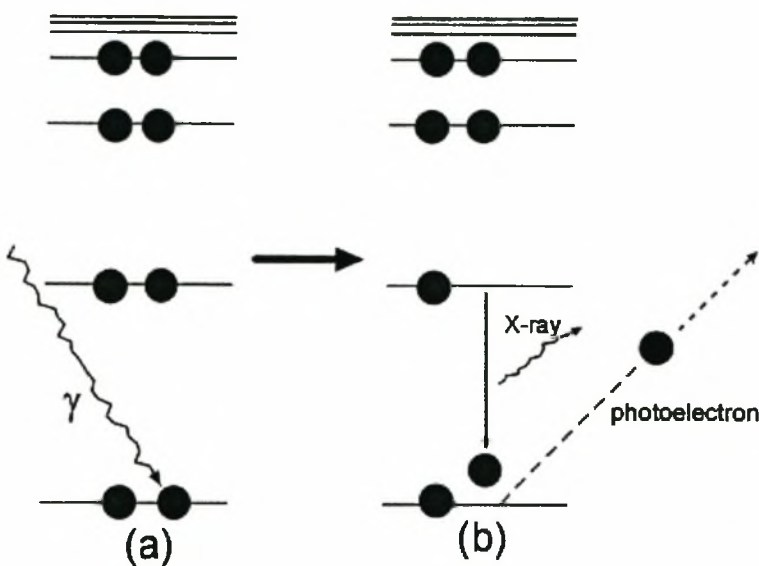


Figure 2.4: Photo-electric absorption

Compton Scattering

Compton scattering or *incoherent scattering* involves a γ -ray and an electron considered to be "free" and "at rest". Contrary to coherent scattering where the γ -ray undergoes an inelastic collision with the electron, here the γ -ray undergoes an elastic collision with the electron. The incident γ -ray with energy $E_0 = h\nu$ is scattered at an angle θ and the

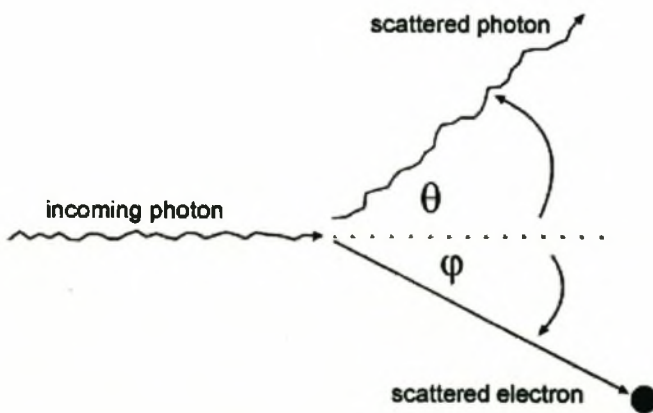


Figure 2.5: Compton Scattering

electron at an angle ϕ with respect to the incident γ -ray's original direction (see figure

2.5). Its initial energy is reduced to $E = h\nu'$ given by eq. 2.20, with the electron receiving the difference between the initial energy of the γ -ray and its final energy (e.q. 2.21).

$$E = \frac{E_0}{1 + \alpha(1 - \cos\theta)} \quad (2.20)$$

$$T_e = E_0 - E \quad (2.21)$$

The energies transferred to the electron form a continuum, because all kinetically allowed scattering angles are possible during Compton scattering. The maximum energy transferred to the electron occurs when the γ -ray scatters at an angle $\theta = \pi$. In this case, $T_e = E_0 - E$ where $E = E_0 \cdot [1 + 2\alpha]^{-1}$. The minimum amount of energy transferred to the electron occurs when the γ -ray grazes the electron ($\theta = 0$). Then $T_e = 0$ and $E \simeq E_0$.

Pair Production

Pair production increases with increasing gamma-ray energy. Gamma-rays with incident energies above 1.022 MeV can undergo pair production in the Coulomb field of the nucleus. In this interaction, the incident γ -ray disappears, and part of the energy of the γ -ray is converted into mass with the creation of an electron-positron pair. The excess energy is shared between the electron and the positron in the form of kinetic energy.

Electron Energy Loss

Spectrometers record the kinetic energy which electrons and positrons lose within the scintillation crystal. Through inelastic collisions, and Coulomb interactions, electrons are slowed and stopped in the crystal.

As the electron passes through a medium it ionizes or excites surrounding atoms. In turn, the attractive and repulsive forces acting on the traveling electron decelerate the electron. During this deceleration, the electron releases radiative energy called bremsstrahlung. The ratio of the specific energy losses is given approximately by:

$$\left(\frac{dE}{dx}\right)_r \cong \frac{ZE}{700} \cdot \left(\frac{dE}{dx}\right)_c \quad (2.22)$$

where E is in MeV and $(dE/dx)_r$ and $(dE/dx)_c$ refer respectively to the radiative and collisional energy losses per unit distance dx [Kno00]. Due to these interactions, the range of electrons in different media is finite. This range is related to the specific collisional and radiative energy losses by [BDLPV74]:

$$R = \int_E^{E_{\min}} \left[\left(-\frac{dE}{dx} \right)_r + \left(-\frac{dE}{dx} \right)_c \right]^{-1} dx \quad (2.23)$$

Alternatively, for computation efficiency, the range of a electron can also be calculated from a formula given by Mukoyama (1976):

$$R = F(E) \cdot \ln 2 \cdot \left[1 + \frac{(Z + 1.2)E}{800 \ln 2} \right] \cdot 8.50 \quad (2.24)$$

where

$$F(E) = 1.5 - 1.3 \exp(-2E), \quad (2.25)$$

is a correction factor [Muk76].

2.4 Environmental Radioactivity

Potassium, uranium, thorium and other radioactive nuclides of interest are measured during a routine radiometric survey. ^{40}K is the sole gamma-emitting isotope of potassium. The estimation of K is thus direct through the detection of its characteristic 1.461 MeV γ -ray [IT03]. Uranium and thorium do not emit measurable γ -rays, so, their daughter products lower down their respective decay chains are used to estimate the concentrations of these elements.

Thorium concentrations are estimated through the detection and measurement of the 2.614 MeV ^{208}Tl daughter isotope γ -ray. Uranium is estimated from the 1.764 MeV ^{214}Bi daughter isotope γ -ray. Unlike potassium, uranium elemental concentration values are calculated to "parts per million of equivalent uranium" (ppm eU) and similarly for thorium (ppm eTh). This is because uranium and thorium are assumed to be in secular equilibrium with the daughter products measured.

2.4.1 Uranium and Thorium

Both uranium and thorium decay to lead through a series of daughter species. Figure 2.6 shows these decay series or decay chains. Uranium has a series of 17 daughter species before it reaches its stable state, ^{206}Pb . As shown in the figure, the isotopes decay via α and β decay. As the reaction proceeds down the chain, α and β decay occur.

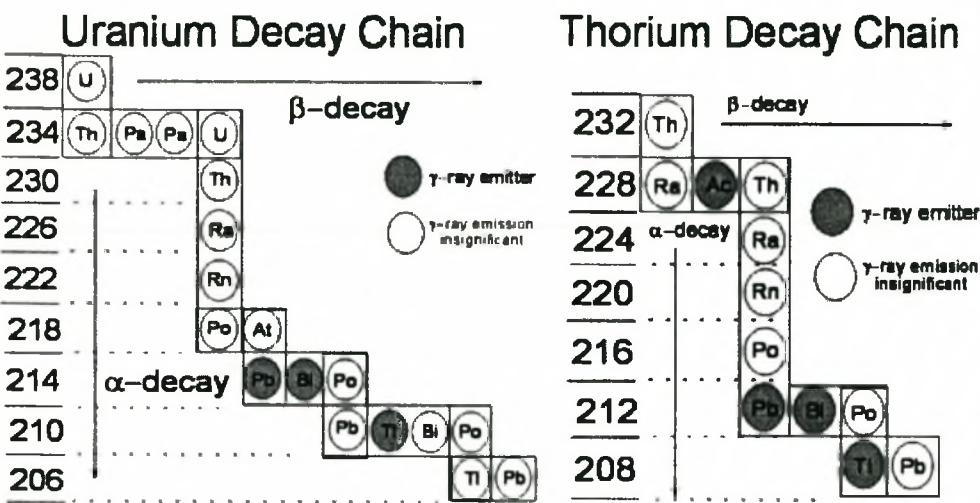


Figure 2.6: Uranium and thorium decay chains [Min97]

As shown in the figure, uranium and thorium themselves do not emit measurable γ -rays. For this reason, the γ -rays emitted by their respective daughters are measured. For terrestrial radioactivity, the three daughter products of uranium, ^{214}Pb , ^{214}Bi and ^{210}Tl emit measurable gamma-rays above 200 keV.

The same holds for thorium. Thorium has ten daughter species in its decay chain before it reaches its stable state, ^{208}Pb . The significant gamma-emitters are ^{228}Ac , ^{212}Pb , ^{212}Bi and ^{208}Tl . The spectral intensity profile of uranium and thorium are shown in figure 2.7.

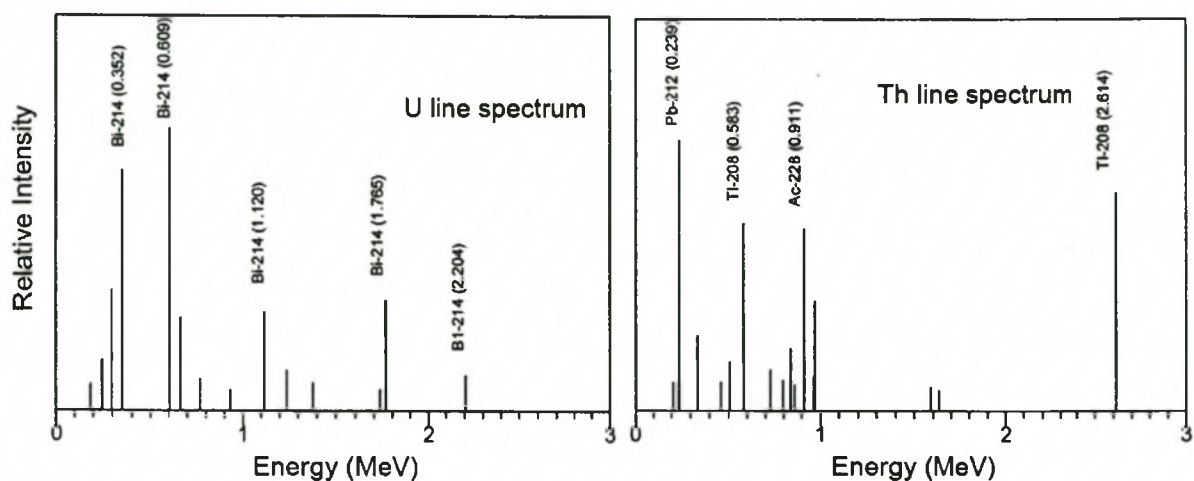


Figure 2.7: Uranium and thorium γ -ray spectral profile

Uranium Disequilibrium

Contrary to thorium, uranium is likely to be in disequilibrium with its daughter products. This is due to uranium being susceptible to removal during hydrothermal alteration or weathering in bedrock [Hal96]. In addition, disequilibrium also occurs when radon gas escapes the surface of the earth through cracks and rock fractures, or when the gas dissolves in groundwater and is thereby removed from the system [IT03].

With respect to airborne gamma-ray spectroscopy, uranium elemental concentration estimates are frequently erroneous. Airborne radiation contributes to these errors. Airborne radon gas not originating from terrestrial uranium is also a parent of ^{214}Bi measured during airborne surveys [Min97, MLB97]. The counts measured for terrestrial radiation are thus corrupted by these airborne radiation sources.

2.4.2 Uranium Parent-Daughter Activities

In a closed system, the activity of daughter species produced during radioactive decay of parent nuclei gradually grows until radioactive or secular equilibrium is reached. When secular equilibrium is reached, the activity of the parent isotope is equal to the activities of all radionuclides in the decay chain. Let λ_i be the decay constant of the i^{th} radionuclide

in the chain. Then:

$$A_1 = \lambda_1 N_1 = \lambda_2 N_2 = \lambda_3 N_3 = \dots = \lambda_i N_i. \quad (2.26)$$

From this relationship the activity of ^{238}U is calculated from the activity of ^{214}Bi . The activity is then related to the concentration of uranium in rock by [IT03]:

$$1\text{ppm U in rock} = 12.35\text{Bq/kg} \quad (2.27)$$

2.5 Airborne Gamma-ray Spectrometry

Airborne gamma-ray spectrometry (AGRS) or radiometrics involves the measurement, mapping and interpretation of the relative concentrations of the earth's natural gamma radiation field. Potassium, ^{40}K , Uranium, ^{238}U , Thorium, ^{232}Th , and their daughter products emit characteristic sets of γ -rays. Measurement of these photons between 0.1 to 3.0 MeV reveal the relative distribution and concentration of these naturally occurring radionuclides in the ground.

2.5.1 Methodology

Airborne radiometric surveys are carried out with scintillation and semi-conductor detectors with their associated electronics mounted inside the aircraft. Gamma radiation measurements from the air over an area are obtained and subsequently the data are processed and presented for interpretation.

A typical airborne radiometric survey usually makes use of two $16l$ detector packs. With the aircraft traveling at 50 to 70 m/s at a constant predetermined height, a spectrometric measurement is recorded every second along with the instantaneous position, velocity relative to the ground, height, temperature and pressure. The aircraft is flown along predefined parallel "flight-lines". The spacing of these flight-lines are between 50 to 400 m. Flight-line spacing and survey height are determined by the needs of the client

CHAPTER 2. GAMMA-RAY SPECTROSCOPY

22

requesting the survey and the terrain being surveyed. A high-resolution survey is normally carried out with a fixed-wing aircraft using a line spacing of 200 m and a height of 100 m.

Following the survey, the recorded data are processed and corrected. Data are corrected for processes not related to the geology of the area surveyed. The concentrations of the radionuclides of interest are calculated from the corrected data. These values are normally presented in the form of 2D maps or sectional profiles.

2.5.2 Detector and Spectrometer

Depending on the survey or application, several types of detectors are used for AGRS. CsI, NaI, BGO or HPGe detectors are commonly used to perform these measurements. Due to its characteristics for γ -ray detection, NaI detectors are popular for airborne radiometric surveys. Thallium-activated sodium-iodide, NaI(Tl), crystals commonly used for surveying typically have a total volume of 16*l*. Each crystal pack consists of four prismatic NaI crystals measuring 40.6 cm \times 10.2 cm \times 10.2 cm. Normally, these crystals are installed in a high-impact aluminum container. Thermal and mechanical shock protection are provided allowing the detectors to be mounted directly on the floor of the aircraft.

Spectrometers currently in use for airborne geophysical surveys, such as the GR-820, provide state-of-the-art hardware and software capabilities. In the energy range of 0.1 to 3.0 MeV, 256 or 512 channels are used to record spectra. Spectrometers can host up to four 16*l* crystal detector packs, providing features such as automatic gain stabilization of individual spectra recorded by each crystal.

2.5.3 Data Processing

Recorded γ -ray spectra use a sample integration time of 1 second. The recorded spectrum is a combination of low activity radiation sources of terrestrial K, U and Th in addition to electronic noise, aircraft radiation and atmospheric gamma radiation, such as the daughter

products of airborne radon gas and cosmic radiation. The components contributing to the spectrum are separated using multichannel processing and smoothing techniques such as NASVD (Noise Adjusted Singular Value Decomposition) and MNF (Maximum Noise Fraction) [AKBH99]. Each contributing component is identified by means of its spectral shape. Aircraft-, background-, airborne- and cosmic radiation are subsequently removed from the spectrum. This complex cleaning process of airborne spectra is necessary due to the low count rate measured for the radionuclides of interest which is typically 25 cts/sec for Th.

After smoothing the data, stripping corrections are applied. Stripping corrections are corrections associated with the scattering of higher energy photons of U and Th recorded in the lower energy channels of K and U. Following the stripping corrections, a height correction is applied to the measured counts of K, U and Th to account for the attenuation of gamma-rays in air. The height is corrected for the ambient temperature and pressure measured during each 1 second recording interval. This is necessary since these parameters influence the density and thus the attenuating properties of the air. Finally, the corrected count rates are converted to ground concentrations of the radioelements by dividing the corrected count rates by the sensitivity of the detector for a particular gamma-ray energy [MLB97]. The sensitivity of the detector for a particular energy can be calculated by means of Monte Carlo methods, experimental data or a combination of the two [AS01, IT03, RBT89].

Chapter 3

Monte Carlo Modelling

Introduction

Gamma-rays are observed with a detector due to the occurrence of predominately three interaction processes with atoms in the medium. These processes, namely scattering, absorption or pair production occur as the photon is transported through the detector crystal. These transport processes can be modeled on a computer to produce a predicted response of the detector to incident gamma-rays.

Detector response functions (DRF) are of importance in radiation detection applications. Information gathered from DRFs are used to determine the extent of absorption, pair production and scattering in the detection medium. Monte Carlo simulation is one method for obtaining DRFs.

Not all features of the detector response can be simulated. Crystal imperfections, detector housing effects and surrounding background radiation are difficult to model. DRFs therefore serve as a guide and are applied in conjunction with experimental response functions [OSLBF00].

Most Monte Carlo programs that simulate the response of radiation detectors model the detector crystal for simplicity of the calculation as either having a spherical or cylindrical geometry. Detectors commonly used in airborne radiation surveys have a rectangular shape. For the energy range 0.1 MeV to 3.0 MeV relevant in environmental applications, Billings and Hovgaard (1999) give the flux density ϕ per unit time recorded by a prismatic

airborne detector at a height h , as:

$$\phi = \int dx \int dy \cdot \frac{1}{4\pi\mu_e r^3} \cdot (hN) d_e \cdot e^{-\mu_a r} \quad (3.1)$$

where μ_e is the mass attenuation coefficient within the earth, μ_a the mass attenuation coefficient within the air, N the number of γ -rays emitted by the source and r the radial distance between the source and position of observation.

d_e describes the detector's sensitivity to record incident γ -rays. According to Billings and Hovgaard, the detector sensitivity is the product of the solid angle of the detector, Ω , as seen by the source and its peak efficiency, ε_p , namely:

$$d_e = \Omega \cdot \varepsilon_p \cdot h^2 = \Omega \cdot [\epsilon \cdot \varepsilon_t] \cdot h^2 \quad (3.2)$$

with ε_t the total efficiency and ϵ the photofraction.

Billings and Hovgaard derive an analytical solution for the sensitivity or response of a rectangular γ -ray detector crystal to a mono-energetic γ -ray which takes into account the change in detector geometry with incidence and azimuthal angle [BH99]. For a detector located at a distance h directly above a point source, the solution is given by:

$$d_e = \frac{abc}{4\pi} \cdot \epsilon \cdot \left[\frac{\varepsilon_{T_{xy}}}{c} \right] = \left(\frac{\epsilon ab}{4\pi} \right) \cdot [1 - \exp(-\mu_d c)] \quad (3.3)$$

where a, b, c is the length, width and height of the rectangular detector, μ_d the attenuation coefficient for the detector material and $\varepsilon_{T_{xy}}$ the total count efficiency for the detector with side parallel to the xy plane. For a rectangular airborne crystal, $a = 40.6$ cm and $b = c = 10.2$ cm. Generally, four of these crystals are used in one detector pack adjacent to each other. The detector dimensions can then be approximated by $a = b = 40.2$ cm and $c = 10.2$ cm.

Their description of the response of the detector to γ -rays contains two important parameters characteristic to a detector material namely the total count efficiency and the photofraction. The total count efficiency is a function of the attenuation coefficient, μ_d , an inherent property of the crystal medium. In their study, the value for the attenuation coefficient of NaI(Tl) for a 2.614 MeV γ -ray is quoted as 0.1485 cm^{-1} . This gives a total

efficiency value of 78% for the detector along its short axis, c . Using the same formula (eq. 3.3) but a different attenuation coefficient of 0.1400 cm^{-1} [AIJ81], the total detection efficiency along the same axis reduces to 76%. Apart from the attenuation coefficient, ϵ_T is also influenced by the height of the detector. Along the long axis, a or b , the total detection efficiency is 99%.

The photofraction is the probability that the γ -ray energy is entirely absorbed by the detector. The photofraction value depends on the γ -ray energy, detector dimensions and the medium that fills the active volume. It does not depend appreciably on the source to detector distance or on the source shape, so that, at each energy, this quantity is characteristic of a given detector [CT89].

Cesana and Terrani [CT89] derived an empirical formula for the photofraction that is valid for any kind of detector material. This formula is based on the detector volume to total surface ratio, V/A , the ratio of the photoelectric absorption coefficient and the total attenuation coefficient, τ/μ , and an appropriate energy dependent coefficient $b_r(E)$ in $[\text{cm}^{-1}]$, and is given by:

$$\epsilon = 1 - \left(1 - \frac{\tau}{\mu}\right) \exp \left[-2.03 \cdot [b_r(E)] \cdot \left(\frac{V}{A}\right) \right]. \quad (3.4)$$

The parameter $b_r(E)$ is calculated in terms of a reference material and in their case the reference material is Ge. The photofraction values they calculated with eq. 3.4 agrees well with experimental values for NaI(Tl) detectors that have V/A ratios between 0.762 to 1.954 in the energy range of 0.3 to 3.0 MeV.

Allyson and Sanderson measured the photofraction in their study of airborne NaI(Tl) detectors and also calculated these values by Monte Carlo simulation and also with eq. 3.4 [AS98]. Their photofraction values from the simulations and those calculated with eq. 3.4 differ by 13% and the simulation value compared to the measurement by 17%. This difference they ascribed to packaging material surrounding the detector crystal which was not included in their calculation. Subsequently, they included this into their transport computer code thereby reducing the difference by 11%. In relation to this, Billings and Hovgaard based their Monte Carlo code on that of Allyson and Sanderson with the main

difference being in the method for tracing the path of the γ -ray to the detector. The photofraction values they use are supported by their Monte Carlo simulations.

The probability that the γ -ray energy will be entirely absorbed by the detector is an inherent property of the detector crystal medium, and should therefore not depend on the detector surrounding material, the source detector distance nor the source distribution. Although, Cesana and Terrani provide an empirical formula to calculate the photofraction, their formula is derived only for detectors with a cylindrical geometry. Additionally, the V/A ratio does not exceed 1.9. The V/A ratio for an airborne sized detector is 3.39. This should influence the photofraction significantly.

With the differences in calculated, simulated and measured photofraction values reported by these authors, the calculation of the photofraction of a large prismatic NaI(Tl) crystal is revisited in this thesis, whereby a new computer program is written. Numerous authors have modeled coupled photon-electron transport. However, these models are largely devoted to cylindrical shapes. Although the transport and interaction kinematics of γ -rays in a medium are not dependent on the geometry of the detector, the volume to surface ratio does influence the absorption of γ -rays in the medium. With respect to eq. 3.4, the exponential decreases with increasing V/A ratios. This results in an increase in γ -ray absorption probability.

For the work contained in this thesis, a Monte Carlo based computer code, called **NIPET** (**NaI Photon Electron Transport**) computes the response of a NaI(Tl) crystal to mono-energetic γ -rays in the energy range 0.1 to 3.0 MeV. This chapter describes the transport models developed and used to simulate the passage of γ -rays and electrons in a rectangular shaped NaI(Tl) crystal.

Public general purpose Monte Carlo source codes are available on the internet. Users are free to order or download, compile and run these sources codes. Additionally, the codes are open to modification to fit the requirements of the end user. To validate the results obtained from the photon-electron transport computer program developed for this thesis, a coupled photon-electron transport Monte Carlo computer code named

DOSRZnrc is used [KR02]. The program was downloaded from the internet, compiled and run on a PIII(667MHz) linux desktop computer. This particular routine of the general purpose photon-electron transport Monte Carlo program **EGSnrc** is specifically written for detectors of cylindrical geometry.

For electron transport, DOSRZnrc solves the Boltzmann transport equation [KR02]. In addition, attenuation coefficients used by the EGSnrc program differ from those used in this thesis. Mild differences in peak and total efficiencies are expected, but the purpose of the EGSnrc code is to validate that the physics related to photon and electron transport in NaI(Tl) is contained and correctly implemented in NIPET.

3.1 The Detector Response Function

The detector response function (DRF) is a probability distribution function defined as the pulse height distribution for an incident monoenergetic γ -ray [SG04]. Normally DRFs are denoted by $D(E', E)$ where E is the incident γ -ray energy and E' the pulse height energy. The DRF is always positive over its entire range and integrates to unity over all energies, E' [GS04, SG04].

This function provides detailed information pertaining to particular constituents or features making up the detector response function. These features include the full energy peak related to the absorption process, single and double escape peaks related to the pair production process and scattering which consists of the Compton saddle and multiple scattering events. Furthermore, features contained in the DRF can be evaluated individually depending on the objective of the study.

In this study, a computer program was written to calculate the detector response function specifically for large prismatic NaI(Tl) crystals used in airborne geophysical radiometric surveys. The efficiency and photofraction values for these large crystals are calculated directly from the detector response function. The results of this Monte Carlo based computer code are then compared to published results of $3'' \times 3''$ cylindrical detector

crystals. In addition, photofraction calculations for large $40.6 \times 40.6 \times 10.2$ cm airborne NaI crystals are compared to those published in the literature.

3.1.1 Efficiency Calculations

Terms and Definitions: To calculate the absolute efficiency of a detector, the geometry of the source needs to be taken into account. The **absolute efficiency** of the source-detector system is then defined as the number of γ -rays interacting with the detector divided by the number of γ -rays generated by the source [CMPP83]. The **intrinsic efficiency** of the detector is defined as the total number of γ -rays interacting with the detector and recording an event divided by the total number of γ -rays impinging on the detector. Similar to the intrinsic efficiency, the **total efficiency**, ε_t , is defined as the total number of γ -rays that interacted in the detector depositing either a fraction or all of their initial energy. Finally, the detector **peak efficiency**, ε_p , is defined as the ratio of number of γ -rays that deposit their full energy in the crystal [Kno00] to the total number of γ -rays impinging on the detector.

In NIPET, all γ -rays, N , tracked in the simulation, start at the base of the detector and are thereby defined as being incident on the detector. A counter is used to keep track of those γ -rays with the primary energy, E_0 , that do not interact with the detector. With this approach, the number of γ -rays incident on the detector is always known and defined by the user. The number of pulses recorded by the detector is then simply the difference between the total number of γ -rays incident on the detector and those that did not interact with the detector crystal. Knowing these values, theoretically, the intrinsic detector efficiency can be calculated as described above.

Generally, the intrinsic efficiency of the detector is tabulated as well as the peak and total efficiencies. From these values, the photofraction can be calculated. Knowing efficiency values of a detector, the absolute activity of radioactive sources can be calculated [PAP04]. Other quantities important in medical physics and environmental physics such as the *kerma* or *Gray* can also be calculated with these values [AM03, SRS02].

3.1.2 Photofraction

The detector photofraction or peak-to-total ratio is an indicator of the full and partial absorption of incident γ -rays by the crystal. It is fundamentally a function of detector size and γ -ray energy [AS98].

The photofraction can be calculated by dividing the peak efficiency by the total efficiency, i.e.:

$$\epsilon = \frac{\epsilon_p}{\epsilon_t} \quad (3.5)$$

In NIPET the detector photofraction is calculated with eq. 3.5 and with the calculated and normalized DRF. From the latter calculation, the DRF integrates to unity and subsequently the photofraction can simply be read off the normalized DRF at the full energy.

Photofraction values for large NaI airborne crystals are limited [AS98, BH99, Pro00]. NIPET primarily addresses this and explicitly calculates the photofraction from eq. 3.5.

3.1.3 Detector Smoothing

The DRF calculated is convolved with a Gaussian function which describes the smoothing process of a real detector to emulate a "real" energy spectrum. The Gaussian function contains the resolution of the detector, a characteristic specific to each detector and detector crystal type [dS01]. The Gaussian function is given by:

$$G(E) = \frac{N}{\sigma\sqrt{2\pi}} \exp\left[-\frac{(E - E_0)^2}{2\sigma^2}\right] \quad (3.6)$$

where N represents the number of counts recorded at E_0 , the incident γ -ray energy, and σ the standard deviation.

3.2 Attenuation Coefficients

To calculate the probability that a γ -ray will interact within a medium, the total attenuation coefficient, μ_t , must be known. The total attenuation coefficient is equal to the

sum of the attenuation coefficients of the different interaction processes, i.e.:

$$\mu_t = \mu_{pe} + \mu_{pp} + \mu_{cs} + \mu_{is} \quad (3.7)$$

where μ_{pe} , μ_{pp} , μ_{cs} and μ_{is} are the photoelectric absorption, pair production, coherent scattering and incoherent scattering attenuation coefficients respectively [Att86]. Generally, the magnitude of μ_{cs} is negligible for photon energies above 100 keV, and can subsequently be omitted in eq. 3.7 [AS98].

The attenuation coefficients for γ -rays are energy dependant. Empirical polynomials were used to compute the γ -ray attenuation coefficient of a particular interaction process for a given photon energy [AIJ81]. For each interaction type, coefficients for second and third order polynomials of the form:

$$\mu = a_0 + a_1 E + a_2 E^2 + a_3 E^3 \quad (3.8)$$

are given; where μ is the attenuation coefficient in cm^{-1} and E the γ -ray energy in MeV. The coefficients a_0, \dots, a_3 were obtained by fitting polynomials to the cross-sections for the absorption coefficients for NaI(Tl) given by Hubbel(1969)[AS98].

3.3 Photon Transport

Gamma-ray transport is simulated in a $40.6 \times 40.6 \times 10.2\text{cm}$ rectangular NaI(Tl) crystal, by choosing for instance the pathlength, interaction process or scattering angle of the γ -ray randomly. Specifically, a particle starts from a particular location and is followed through the interacting medium. The history is terminated when the particle has lost all its incident energy in the medium or when it escapes the medium or when its energy has decreased to less than 10 keV.

3.3.1 Geometrical Tracking

As illustrated in figure 3.1, the origin of the Cartesian coordinate system is chosen at a corner of the rectangular medium, with the positive x -axis corresponding to the length,

the positive y -axis corresponding to the width and the positive z -axis corresponding with the height of the crystal. The base of the crystal spans the $x - y$ plane.

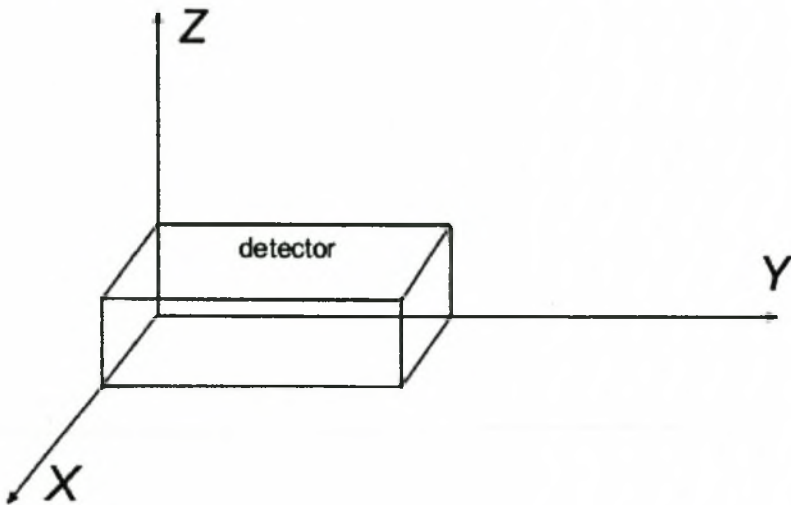


Figure 3.1: Coordinate system and detector orientation

The program allows for two initial coordinate options. The γ -ray either starts from a user-defined position or a random position in the X-Y plane. The coordinates of its initial position are given by:

$$x = \xi_x \cdot X \quad (3.9)$$

$$y = \xi_y \cdot Y \quad (3.10)$$

$$z = 0 \quad (3.11)$$

where the variables ξ_x, ξ_y are either fixed or $\in [0, 1]$. X and Y are the length and width of the detector respectively. The initial directional cosines defined for a vector \vec{k} as $\vec{k} = k_x \hat{x} + k_y \hat{y} + k_z \hat{z}$ are determined by:

$$k_x = \sin \theta \cdot \cos \phi \quad (3.12)$$

$$k_y = \sin \theta \cdot \sin \phi \quad (3.13)$$

$$k_z = \cos \theta \quad (3.14)$$

where the angles, ϕ and θ , are determined with the aid of two random variables, ξ_ϕ and ξ_θ as follows:

1. The azimuth angle is determined by:

$$\phi = 2\pi \cdot \xi_\phi \quad (3.15)$$

2. The polar angle is determined by:

$$\cos \theta = \xi_\theta \quad (3.16)$$

With the initial start position and flight direction known, by means of vector algebra the distance to the closest boundary in the direction of \vec{k} is calculated. The vector equation:

$$\vec{B} = \vec{p} + D \cdot \vec{k} \quad (3.17)$$

is solved for D where \vec{B} is the equation of the closest boundary in the direction of \vec{k} and \vec{p} the particle's Cartesian coordinates in \mathbb{R}^3 .

Two reference frames are now introduced and shown in figure 3.2. The "laboratory frame" and the "photon frame". The "laboratory frame" is fixed in space and corresponds to the fixed coordinate system defined earlier. The "photon frame" moves relative to the laboratory frame. Initially the photon frame's x-, y- and z-axes are aligned parallel to the X-, Y- and Z-axes of the laboratory frame.

Following an interaction, the photon frame is translated and rotated relative to the laboratory frame. The photon's new directional cosines now need to be transformed back to the laboratory frame. The resultant directional cosines, relative to the laboratory

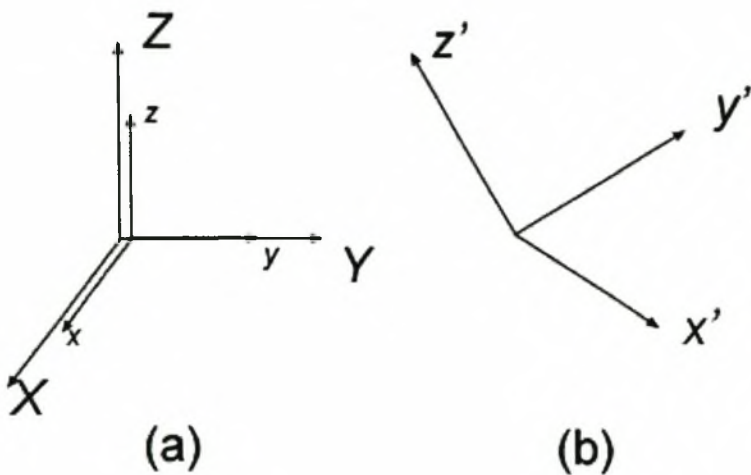


Figure 3.2: Laboratory frame and photon frame

frame after an interaction event, are calculated using the rotation matrix:

$$M_{\text{rot}} = \begin{pmatrix} \cos\theta \cos\phi & -\sin\phi & \sin\theta \cos\phi \\ \cos\theta \sin\phi & \cos\phi & \sin\theta \sin\phi \\ -\sin\theta & 0 & \cos\theta \end{pmatrix} \quad (3.18)$$

The new directional cosines for a γ -ray with an arbitrary incident direction (k_x, k_y, k_z) scattered in a direction θ_s, ϕ_s are then given by:

$$\begin{aligned} k'_x &= k_x \cos\theta_s + \sin\theta_s(k_z \cos\phi_s \cos\phi_s - \sin\phi_s \sin\phi_s) \\ k'_y &= k_y \cos\theta_s + \sin\theta_s(k_z \cos\phi_s \sin\phi_s - \sin\phi_s \cos\phi_s) \\ k'_z &= k_z \cos\theta_s - \sin\theta_s(\sin\theta_s \cos\phi_s) \end{aligned} \quad (3.19)$$

3.3.2 Pathlength

The photon moves from its initial position P to its calculated interaction point P' . For the γ -ray with a particular energy, the total attenuation coefficient, μ_t , is calculated first. The probability of a γ -ray traveling a distance d is given by:

$$p(d) = 1 - \exp(-\mu_t d) \quad (3.20)$$

where d is the pathlength of the γ -ray [BWGV78, BH99]. To determine the interaction point of the γ -ray, the pathlength of the γ -ray must be known. The pathlength is determined by setting a random variable $\xi_{ip} \in [0, 1]$ equal to the interaction probability, $p(d)$, where upon eq. 3.20 is solved for d [Pro79, Zai99]:

$$d = \frac{-\ln(1 - \xi_{ip})}{\mu_t} \equiv \frac{-\ln(\xi_{ip})}{\mu_t} \quad (3.21)$$

Using d , the interaction point \vec{P}' is determined with eq. 3.17 by replacing \vec{B} by \vec{P}' and D with d . Following an interaction, the next interaction point is determined and updated using:

$$\vec{P}'' = \vec{P}' + D' \cdot \vec{k}' \quad (3.22)$$

where D' is the new distance to the closest boundary at \vec{P}' in the direction of \vec{k}' given in eq. 3.19. The program tests whether the interaction point \vec{P}' is within the volume of the interacting medium; in this case NaI(Tl). If \vec{P}' is within this volume, the program continues; otherwise the history is terminated and a new history is started.

3.3.3 Photon Interaction

The interaction probability, $P(D)$, is determined by eq. 3.20, but with d , the γ -ray pathlength, replaced by D , the distance to the closest boundary. A random variable $\xi_t \in (0, 1)$ is used to determine whether an interaction takes place or not. An interaction takes place if

$$\xi_t < P(D) \quad (3.23)$$

is satisfied, otherwise the history is terminated and the γ -ray is considered to have escaped the medium without interacting. If eq. 3.23 is true, the program chooses the interaction type with a second random variable $\xi_{it} \in (0, 1)$. Knowing that the photon will interact within the medium before it reaches the boundary, the program first determines whether:

$$\xi_{it} < \frac{\mu_{pe}}{\mu_t} \quad (3.24)$$

is satisfied for photoelectric absorption to take place. If eq. 3.24 is not satisfied, the program calls for a new random variable ξ'_{it} . For Compton scattering (incoherent scattering) to take place,

$$\xi'_{it} < \frac{\mu_{is}}{\mu_{is} + \mu_{pp}} \quad (3.25)$$

must be satisfied. If eq. 3.25 is not satisfied, pair production takes place.

Photoelectric Absorption

If the photon undergoes photoelectric absorption, all the energy is passed on to the electron and the electron transport method described in section 3.4 is used to determine the energy deposited in the interacting medium. Following a photoelectric absorption event, the history of the photon is terminated and the program waits for the electron transport calculation to be completed before it starts a new history.

Compton scattering

When Compton scattering takes place, the polar angle of scattering, θ_s , is determined by random sampling of the Klein-Nishina distribution. Let $E_0 = h\nu$ and $E = h\nu'$ denote the energy of the incoming photon and the energy of the scattered photon respectively. Then

$$\eta = \frac{E}{E_0} = \frac{1}{1 + \alpha(1 - \cos \theta_s)} \quad (3.26)$$

where $\alpha = E_0/(m_e c^2)$. The Klein-Nishina differential cross-section per atom is then given by:

$$\frac{d\sigma}{d\eta} = \pi r_e^2 \frac{m_e c^2}{E_0} Z \left[\frac{1}{\eta} + \eta \right] \left[1 - \frac{\eta \sin^2 \theta_s}{1 + \eta^2} \right] \quad (3.27)$$

with

$$\eta \in \left[\eta_0 = \frac{1}{1 + 2\alpha}, 1 \right] \quad (3.28)$$

where r_e is the classical electron radius, Z the atomic number and $m_e c^2 = 0.511$ MeV.

Eq.(3.27) can be factorized to become:

$$\frac{d\sigma}{d\eta} \simeq \left[\frac{1}{\eta} + \eta \right] \left[1 - \frac{\eta \sin^2 \theta_s}{1 + \eta^2} \right] = f(\eta) \cdot R(\eta) \quad (3.29)$$

where the rejection function $R(\eta)$ has the property $0 < R(\eta) \leq 1$. Furthermore, $f(\eta)$ can be written as:

$$f(\eta) = N_1 \cdot \left(\frac{1}{\eta \cdot N_1} \right) + N_2 \cdot \left(\frac{\eta}{N_2} \right) = N_1 \cdot f_1(\eta) + N_2 \cdot f_2(\eta) \quad (3.30)$$

where $f_1(\eta)$ and $f_2(\eta)$ are probability density functions on $\eta \in [\eta_0, 1]$ and

$$N_1 = \int_{\eta_0}^1 \frac{1}{\eta} d\eta = \ln(1/\eta_0) \quad (3.31)$$

$$N_2 = \int_{\eta_0}^1 \eta d\eta = \frac{1}{2} \cdot (1 - \eta_0^2) \quad (3.32)$$

$$\Rightarrow \frac{d\sigma}{d\eta} \sim [N_1 \cdot f_1(\eta) + N_2 \cdot f_2(\eta)] \cdot R(\eta) \quad (3.33)$$

The polar angle, θ_s , with respect to the incoming photon is determined with the aid of three random numbers ξ_1, ξ_2 and ξ_3 uniform in $[0,1]$ as follows:

1. ξ_1 is used to determine whether $f_1 \cdot R$ or $f_2 \cdot R$ is used in the calculation. If $\xi_1 < N_1/(N_1 + N_2)$, then f_1 is selected, else f_2 is used;
2. ξ_2 is used to sample η from the distributions f_1 or f_2 :
for $f_1 : \eta = \exp(-N_1 \cdot \xi_2)$;
for $f_2 : \eta = \sqrt{\eta_0^2 + \xi_2 \cdot (1 - \eta_0^2)}$;
3. Using $\eta, \sin^2 \theta = t \cdot (2 - t)$ is calculated, where $t = (1 - \eta)/(\alpha\eta)$;
4. η is accepted if $\xi_3 \leq R(\eta)$. If this inequality is not satisfied, the program returns to step 1.

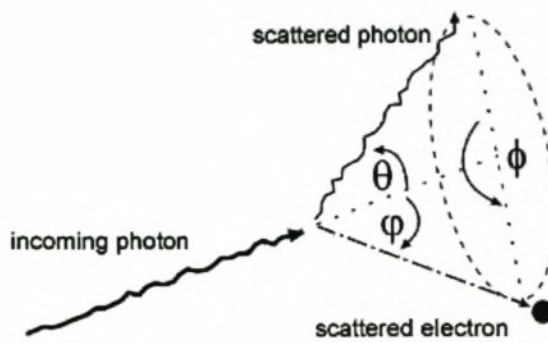


Figure 3.3: Polar and azimuthal angles following Compton scattering

Once η is determined, θ_s is calculated from eq. 3.26 and E is obtained [Mai02]. Subsequently, ϕ_s is chosen isotropically. With θ_s and ϕ_s known, the new directional cosines in the laboratory frame are calculated with eq. 3.19. The kinetic energy transferred to the electron is simply the difference between the initial photon energy and the scattered energy, i.e.:

$$T_{e^-} = E_0 - E \quad (3.34)$$

Assuming that scattering of the photon off an "unbound, free" electron takes place in one plane, the azimuthal angle of the scattered electron is (see figure 3.3):

$$\phi'_{e^-} = \phi_s + \pi \quad (3.35)$$

and the scattered angle relative to the incoming photon is given by:

$$\cot \varphi = (1 + \alpha) \tan \frac{\theta_s}{2} \quad (3.36)$$

When a γ -ray undergoes multiple scattering, the energies passed to the scattered electrons are summed after the γ -ray is finally absorbed, or when the γ -ray escapes from the medium.

Pair Production

If the γ -ray undergoes pair production, an electron-positron pair is created. When the positron collides with an electron, two annihilation γ -rays are generated, each with an

energy of 0.511 MeV. The azimuthal and polar angles of the first annihilation γ -ray are chosen using eq. 3.15 and eq. 3.16. The γ -ray's directional cosines are calculated with eqs. 3.12 - 3.14. The directional cosines of the second γ -ray are then taken to be the negative of the first γ -ray's directional cosines [PGV94].

The first annihilation γ -ray is followed and if it undergoes photoelectric absorption, the energy imparted to the photoelectron is added to the kinetic energy of the positron-electron pair, provided the electron loses its kinetic energy within the medium. If it is scattered, the γ -ray is tracked until it escapes the medium or it loses all its energy. The kinetic energies received by the electrons during these multiple scattering events are added together to determine the total energy deposited in the medium. The second annihilation γ -ray is treated in exactly the same way as the first γ -ray.

3.4 Electron Transport

Electron transport is treated similarly to γ -ray transport as described in the previous section. The major difference between the two transport models is the introduction of the Coulomb interaction between the charged electrons and the surrounding atoms. In the medium, the electrons have a definite range that they can travel before losing all their kinetic energy, whereas in the photon transport model the pathlength is determined randomly.

In this transport model, several simplifications have been made. The electrons are assumed to travel in straight lines and their ranges are considered to be of the order of 1mm/MeV. Furthermore, scattered electrons are not allowed to scatter off the surrounding atoms or electrons, so that electron cascades or electron showers are not permitted. Due to the size of a typical airborne NaI(Tl) crystal, electron leakage is assumed to be negligible and is therefore not considered to affect the calculations. More sophisticated theoretical and analytical models treat electron transport more accurately [DJT00, Zai99].

3.4.1 Geometrical Tracking

Electrons are followed in the medium similar to the way photons are followed described in section 3.3.1. Once its location and directional cosines are known, the distance to the closest boundary is calculated. With the kinetic energy, T , of the incident electron known, the range of this particle is calculated from [Muk76]:

$$R = F(T) \cdot \frac{1}{\rho} \cdot \ln 2 \left[1 + \frac{T}{E_c \ln 2} \right] \cdot 8.50 \text{ cm} \quad (3.37)$$

where ρ is the density of the medium, the critical energy

$$E_c = \frac{800}{Z + 1.2} \text{ MeV} \quad (3.38)$$

is defined as the energy at which the ionization loss due to collision with electrons is equal to the radiative energy loss during deceleration of the electron in the medium and the function $F(T)$ is a correction factor given by:

$$F(T) = 1.5 - 1.3 \exp(-2T) \quad (3.39)$$

with T defined as above [Muk76].

The range, R , of the electron is compared to the distance to the closest boundary calculated with eq. 3.17. If $R < D$, the electron is assumed to have lost all its kinetic energy in the medium. Should the contrary be true, the initial kinetic energy of the electron is discarded. In this case, the electron is considered to have leaked from the medium without depositing any of its kinetic energy in the medium. In the case of positrons, the same energy loss model is applied, but in this case, the coordinate at the end of the positron's track is recorded and used as the start coordinates of the annihilation γ -rays.

3.4.2 Determination of Initial Coordinates and Directional Cosines

As mentioned earlier, the electron transport method is used to determine the energy deposited in the crystal after a γ -ray interaction with bound or free electrons occurs

in the case of photoelectric absorption and Compton scattering respectively. When a photoelectric event occurs, the initial electron position is defined as the interaction point of the γ -ray. The polar [eq. 3.15] and azimuthal [eq. 3.16] angles of the photo-electron are determined randomly. Subsequently, the initial directional cosines are calculated.

For Compton scattering events, the initial coordinates of the electron are also defined at the interaction point. The Compton-electron's azimuthal angle is given by eq. 3.35 and its polar angle by eq. 3.36, from which the directional cosines are calculated [eqs. 3.12 - 3.14]. For pair production, the polar angles are determined using the kinetic energies of the electron and the positron [BDLPV74].

Following pair production, the kinetic energy, $T = E_\gamma - 1.022\text{MeV}$, is randomly distributed between the electron and positron:

$$T_{e^-} = \xi_T \cdot T \text{ and } T_{e^+} = T - T_{e^-} \quad (3.40)$$

where $\xi_T \in [0, 1]$. From Belluscio *et. al.* [BDLPV74], the polar angles of the electron-positron pair are then given by:

$$\theta_{-,+} = \tan^{-1} \left(\frac{m_e c^2}{T_{-,+}} \right) \quad \text{for } E_\gamma \approx 1.022 \text{ MeV} \quad (3.41)$$

and

$$\theta_{-,+} = \frac{m_e c^2}{T_{-,+}} \quad \text{for } E_\gamma \gg 1.022 \text{ MeV} \quad (3.42)$$

The azimuthal angles of the charged pair are chosen randomly using eq. 3.15.

3.4.3 Bremsstrahlung

In this Monte Carlo simulation, the production of bremsstrahlung from the radiative losses of electrons as they transverse the medium is not considered. Although these γ -rays can escape the medium, particularly in the event of high energy gammas, it is assumed that the volume of the medium is large enough to absorb most γ -rays.

3.5 Simulation Algorithm and Flow Diagram

The following is a description of the complete Monte Carlo algorithm employed in NIPET. The program is written in JAVA and consists of ten classes. Each class performs a specific task primarily related to the physics that takes place during the simulation. In this way, corrections and maintainance of the complete program is simplified.

As an example, the class Geometry is given the physical dimensions of the crystal by the user. This class is then used to determine whether the γ -ray is still within the volume of interest. Additionally, it calculates the distance to the closest boundary, and the coordinates of the exit point, should the γ -ray escape this volume. Other classes, such as PhotonTransport, ElectronTransport or ComptonScatter perform tasks as their class names suggest.

After the user gives inputs of the mono-energetic γ -ray, the dimensions of the detector crystal and the number of histories (photons) to track, NIPET requests the user to choose the photon launch position or a random launch position. In order to produce a DRF and subsequently calculate the parameters of interest, the following steps are performed by NIPET (see figure 3.4):

1. Calculate the initial directional cosines k_x , k_y and k_z ;
2. Calculate the attenuation coefficients, μ_{pe} , μ_{pp} , μ_{cs} and μ_t with energy E_0 if the γ -ray begins its history or E after a scattering event;
3. Calculate the exit point and the distance, D , to the closest boundary in the direction of $\vec{k} = \langle k_x, k_y, k_z \rangle$ or \vec{k}' after scattering;
4. Determine the γ -ray pathlength, d ;
5. Determine where the interaction point is located with d ;
6. Test whether the interaction point is within the volume of interest;

7. Discard the history if the interaction point is outside the volume and increase the non-interacted γ -ray counter; otherwise continue;
8. Calculate the interaction probability, $P(D)$ (eq. 3.20);
9. Request a random number, ξ and test whether $\xi < P(D)$ (eq. 3.23);
10. Continue program if the test is satisfied, otherwise discard history, increase the non-interacted photon counter and start a new history;
11. Calculate the coordinate where an interaction will take place with eq. 3.17 and using d as the pathlength;
12. Determine the interaction type as described in section 3.3.3;
13. Determine the amount of energy retained by the γ -ray, E , and that passed on to the electron, T ;
14. Compute the quantity of energy, T' , deposited in the crystal described in section 3.4;
15. Determine whether the γ -ray energy $E < 0.01$ MeV;
16. If step 15 is satisfied, start a new history, otherwise calculate the new directional cosines, \vec{k}' , of the photon and return to step 2.

NIPET outputs four data files containing the average intrinsic efficiency, peak counts, total counts and photofraction calculated for the energies simulated. It also produces a data file containing the normalized counts per energy bin; an energy bin spans 10 keV. This is effectively the detector response function. All data generated during the simulation are also plotted for the user. There are linear as well as logarithmic plots of detector response functions, photofractions and intrinsic efficiency. Additionally, the enlarged Compton continuum is also included in the output plots.

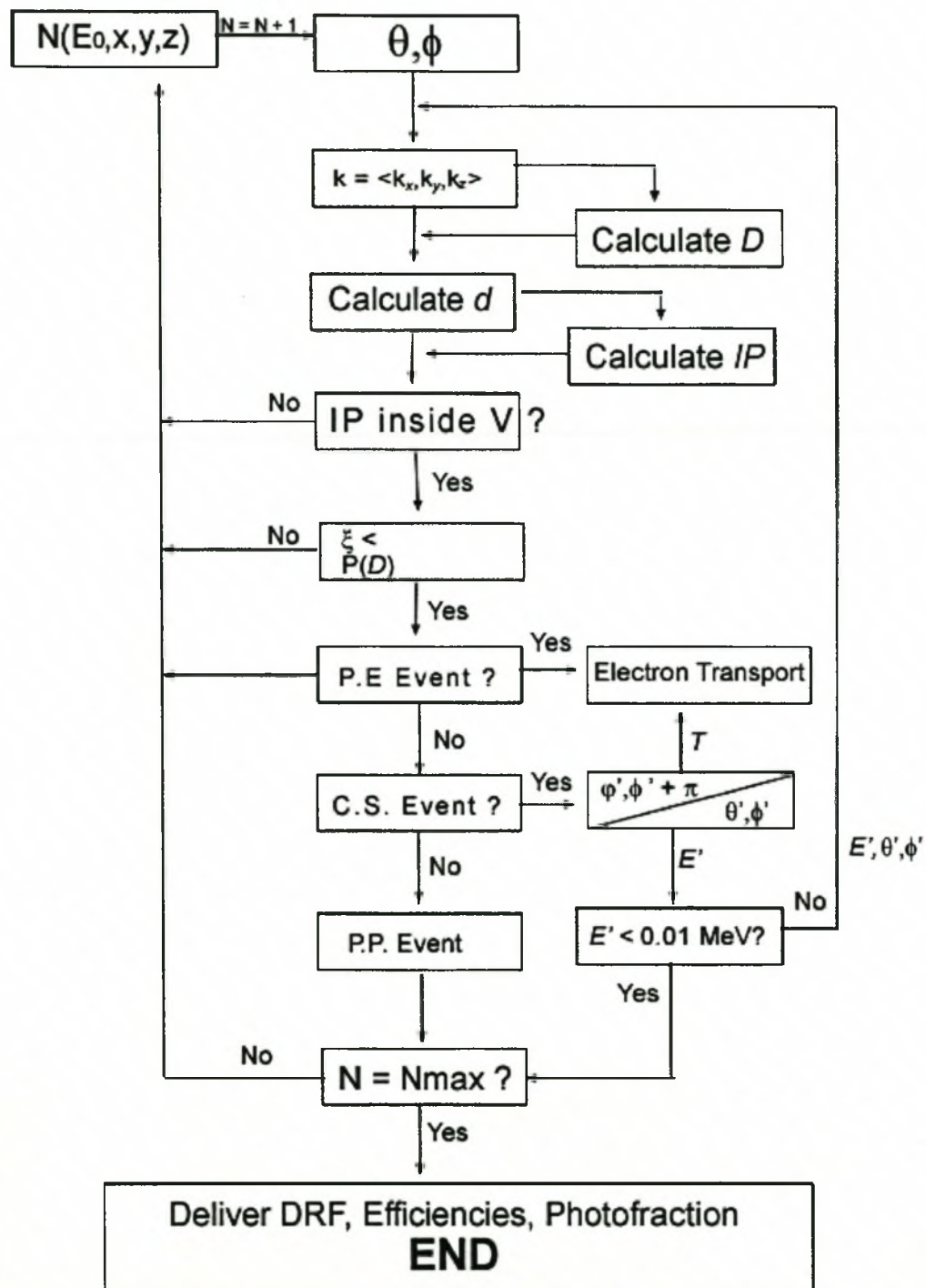


Figure 3.4: NIPET program flow diagram

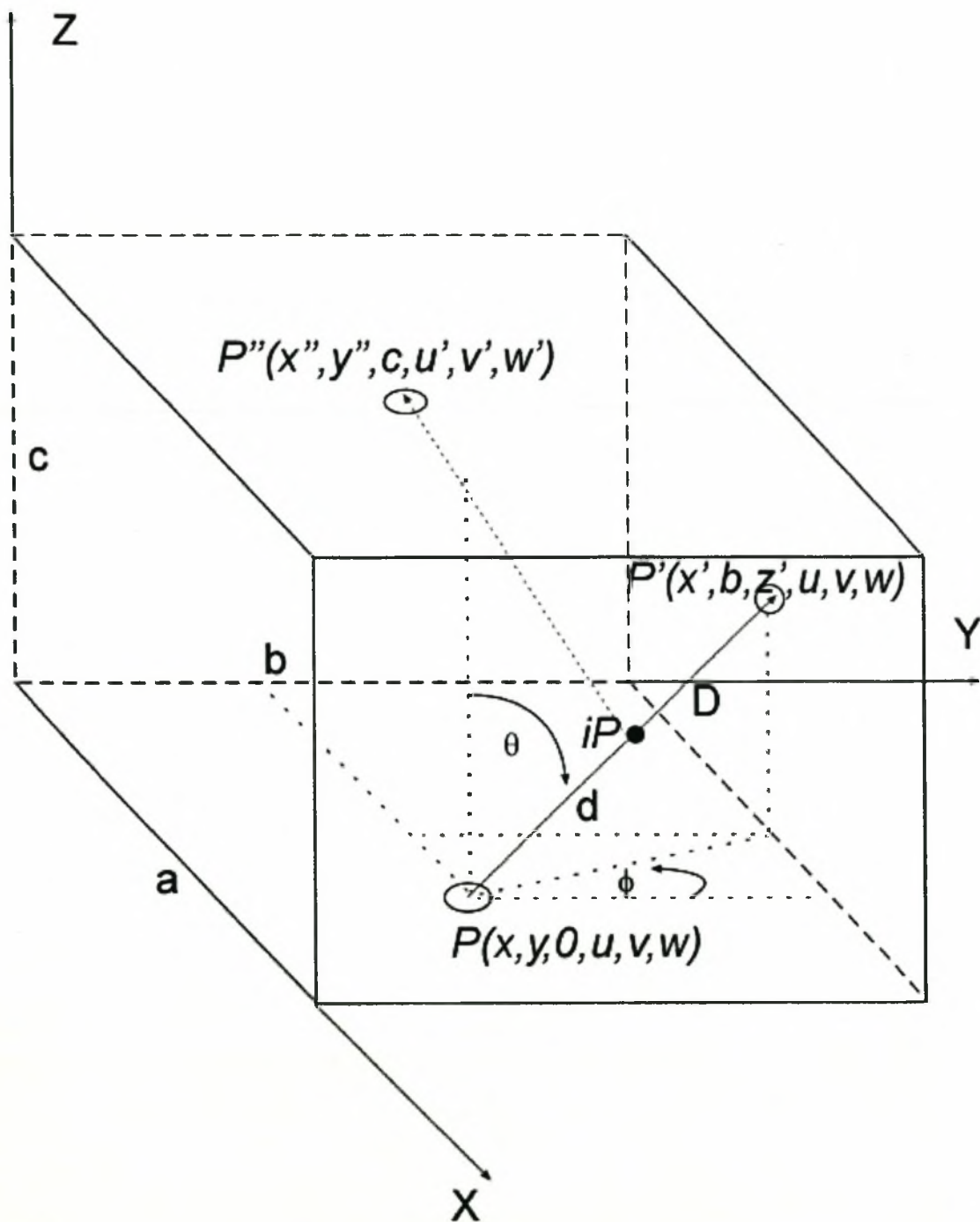


Figure 3.5: Graphical representation of photon transport in NIPET

Chapter 4

Results and Discussion

This chapter is divided into three parts. The first section is primarily devoted to the results generated by NIPET. The section begins with a brief validation of this transport code by comparing it to the general purpose photon-electron transport code, EGSnrc [KR02]. Differences and similarities are briefly discussed. Graphic profiles of DRFs and photofractions of mono-energetic γ -ray input sources for small, intermediate and large prismatic detectors are shown. Additionally, comparative charts for these detector sizes are shown and briefly discussed.

The second part is devoted to a discussion pertaining to prominent features arising from the response of the crystal to low energy γ -rays in comparison with high energy γ -ray sources. The discussion is taken further by looking at the photofractions calculated by NIPET for a small prismatic detector and compared to those given in the literature. Additionally, the response of large detectors is discussed in relation to that of small detectors.

The chapter concludes with a brief discussion of a measured airborne spectrum. The spectra contained in this section were generously donated for this study by GPX Namibia, a geophysical airborne survey company. Spectra are shown before and after processing. These spectra also indicate the contribution of airborne radiation. The removal techniques used for such contaminants are also briefly mentioned.

4.1 Response Function Comparisons

4.1.1 DOSRZnrc compared with Measurement

Two γ -ray calibration sources were measured in the laboratory. The γ -ray source was placed 30.0 cm away on the cylindrical axis of the detector (see figure 4.1). No shielding was used during the acquisition period of 420 seconds. Three measurements were taken. Following each measurement, a 420 second background measurement was also recorded. The three measurements for each source were summed. The mean was computed for each source and background. Subsequently, the mean background was subtracted from the mean spectrum for both the two γ -ray sources, ^{60}Co and ^{137}Cs . The detector used for the

Detector	KEM, NaI(Tl) scintillation detector with ORTEC model 266 PM base
Pre-Amp	ORTEC model 113 pre-amplifier
HV	ORTEC model 456 HIGH VOLTAGE POWER SUPPLY (set to 900V for detector)
Amplifier	ORTEC model 450 research amplifier
Computer	Pentium-MMX, 200 MHz
MCA	Model 9308 MEMORY BUFFER CARD by SILENA INTERNATIONAL S.p.A.
Software	EMCA 2000, MCA EMULATION SOFTWARE by SILENA INTERNATIONAL S.p.A.

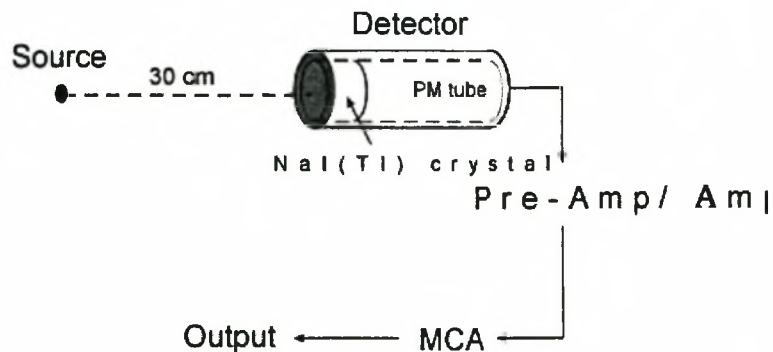


Figure 4.1: Experimental set-up and instrument specifications

measurements consists of a 5.0×3.0 cm NaI(Tl) crystal housed in a cylindrical aluminium casing. The crystal is mounted directly on the entrance window of the detector on a thin film of Havar (a high-strength, non-magnetic material). The photomultiplier tube (PM) is attached directly to the back-end of the detector crystal. The two sources used are disc-like with an average diameter of 0.4 cm. At 30 cm from the detector, these sources effectively represent point sources.

A user-code available in EGSnrc, DOSRZnrc, simulates the passage of an electron or γ -ray in a cylindrical geometry emitted from a point source or parallel pencil beam [KR02]. The energy deposited within an arbitrary volume, defined by the user, is calculated.

After the simulation a statistical analysis of the energy stored in the chosen volume is performed.

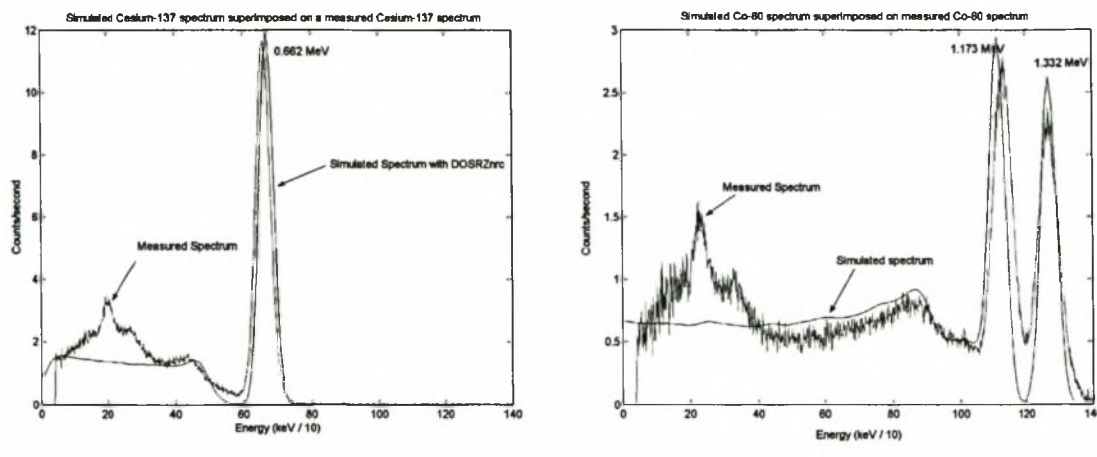
The user specifies the simulation in terms of the geometry, the material composition of the geometric volume, the number of histories, the time limit and the statistical accuracy desired. In addition, the user is free to choose mono-energetic sources or energy spectra containing the energies of the γ -ray(s)/electron(s) and their corresponding intensities. Point sources or parallel beam sources can also be selected.

A ^{60}Co and ^{137}Cs energy spectrum were used as point source inputs. The cylindrical geometry consisted of two media, a 5.0×30.0 cm column of air followed by a 5.0×3.0 cm NaI(Tl) crystal. The pulse height distribution of the whole volume was calculated and plotted as a response function. This function was subsequently convolved with a Gaussian function, the resolution function of the detector.

Analysis

Figure 4.2 displays the results of the simulations compared with the measured spectra of ^{60}Co and ^{137}Cs . There is good agreement between the measurements and the Monte Carlo simulations. For both cesium and cobalt, the simulations reproduce the prominent features evident in the γ -ray spectra. These are the full energy peak at 0.662 MeV in the case of cesium and 1.173 MeV and 1.332 MeV peaks for cobalt, the height of the Compton saddle and the location of the Compton edge. The large backscatter peak visible in the measured spectrum, is absent in the simulated spectra. Gamma-rays scattered at angles between 140° and 180° retain an energy between 200 - 300 keV. They are subsequently photo-electrically absorbed giving rise to this 'backscatter' peak.

In both simulations, the surrounding material was not included. Under these ideal conditions, no backscatter peak should be expected in the simulated spectrum. Additionally, in both figures 4.2(a) and 4.2(b), the valley between the Compton edge and the full energy peak for cesium is deeper in the simulation. This is also apparent in the cobalt simulated spectrum between the two full energy photopeaks. Two arguments can



(a) Cesium spectrum

(b) Cobalt spectrum

Figure 4.2: Simulated cobalt and cesium spectra superimposed on measured spectra

be made. In the case of cesium, the number of multiple scattering events simulated is significantly less than is actually the case in an experiment. This should hold for cobalt as well. A second argument is the omission of the surrounding material in the simulation. During the γ -ray's flight from source to detector crystal, the grazing of γ -rays off free electrons in the thin Havar material can slightly reduce the energy carried by the incident γ -ray.

4.1.2 NIPET compared with DOSRZnrc

The result above confirms that the EGSnrc transport code was implemented correctly on the computer and that satisfactory results are generated after a simulation.

With respect to the photon-electron transport code written for this thesis, EGSnrc was used to verify the pulse height distributions generated by NIPET. Good agreement between the two codes indicates that the particle transport model employed by NIPET is valid. Also, it confirms that the physics governing this transport model is correctly implemented in the code.

NIPET is written to investigate prismatic NaI(Tl) crystals, particularly for large geometries. The user-code DOSRZnrc investigates NaI(Tl) crystals of cylindrical dimen-

sions. According to the formula of Cesana and Terrani (eq. 3.4), the two transport codes should effectively produce the same peak-to-total ratio provided the attenuation coefficients are the same and the volume-to-surface ratio is similar. These are the only parameters that will influence the peak-to-total ratio. From this point of view, the result produced by NIPET can be matched to that produced by DOSRZnrc.

Two sources were simulated with EGSnrc; these are the 0.662 MeV γ -ray of cesium, and the 2.614 MeV γ -ray of ^{208}Tl , a daughter product of ^{232}Th . For DOSRZnrc, for the cylindrical crystal the diameter was set to 7.62 cm and the height to 7.62 cm. The point source was placed 0.1 cm in front of the crystal (This distance is the minimum default distance that can be used), with no air in between. 100000 histories were followed. The dimensions of the prismatic crystal given to NIPET was $7.62 \times 7.62 \times 7.62$ cm for the length, width and height of the crystal. 100000 histories were also followed. For each code, ten simulations were performed. The average of these simulations was then taken and plotted for comparison.

Analysis

Figure 4.3 shows the results produced by the two codes convolved with an appropriate gaussian function. The two codes reproduce the response function of a NaI(Tl) crystal to a mono-energetic γ -ray. For both energies, the full-energy peak, the Compton saddle, Compton edge as well as Compton drop-off due to multiple scattering events are represented. In the case of the high-energy 2.614 MeV spectrum, the emergence of the double and single escape peaks feature prominently as well. As expected, no backscatter peak is visible in both simulations. In both cases, for the 0.662 MeV spectrum and the 2.614 MeV, these distinguishing spectrometric features coincide.

Analysis of both spectra validates the particle transport model used for photons and that used for electrons in the NIPET code. The differences between the two codes are in the height of the Compton saddle, the two escape peaks and full energy peak. These differences can be ascribed to the difference in geometries of the two crystals, but, this is

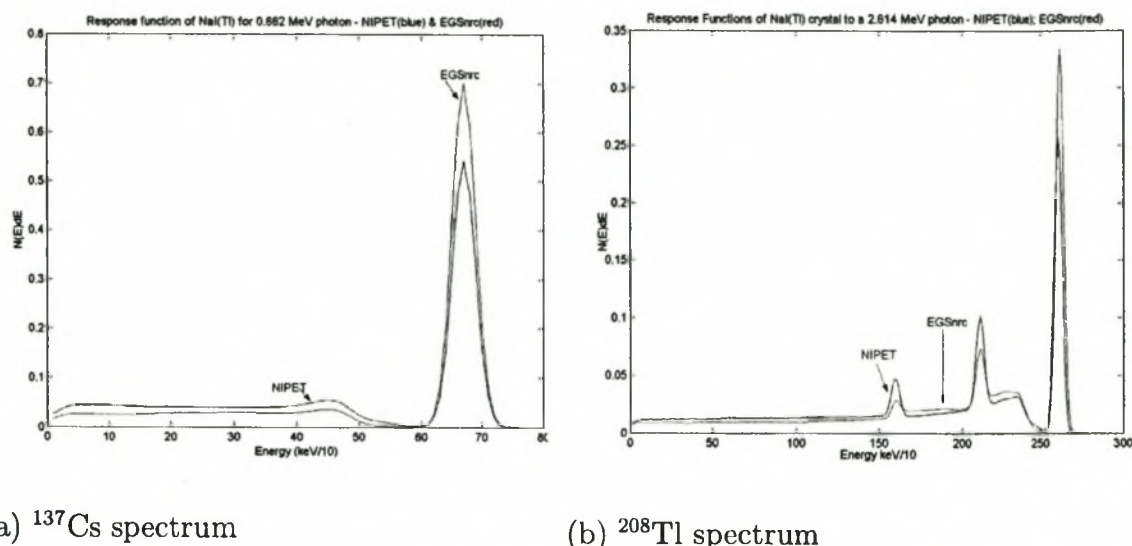


Figure 4.3: Simulated (a) cesium and (b) thallium spectra

unlikely, because according to the Cesana and Terrani formula, both geometries have the same volume-to-surface ratio. An alternative explanation is the different photo-electric absorption coefficients and total attenuation coefficients used by the two codes. This is evident from the EGSnrc 0.662 MeV spectrum, where the full energy peak differs by nearly 30%. For the high energy spectrum the difference in the full energy absorptions peaks is also by the same margin.

4.1.3 Response Functions For Different Crystal Dimensions

For the two isotopes, ^{137}Cs and ^{208}Tl , the DRFs for crystals with the following dimensions were computed (see figure 4.4):

1. $7.62 \times 7.62 \times 7.62$ cm³
 2. $40.6 \times 10.2 \times 10.2$ cm³
 3. $10.2 \times 10.2 \times 40.6$ cm³
 4. $40.6 \times 40.6 \times 10.2$ cm³
 5. $40.6 \times 10.2 \times 40.6$ cm³

CHAPTER 4. RESULTS AND DISCUSSION

52

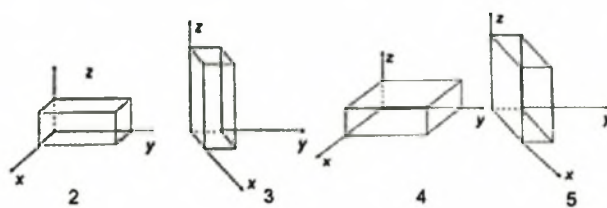


Figure 4.4: Crystal orientations for the airborne detector

The isotopes were chosen for comparison purposes with the published literature. The response functions for the first crystal size are shown in figure 4.3. The dimensions for 2 and 3 are the same, but the orientation of the crystal is different. This is also the case for 4 and 5. The orientations should not influence the DRFs dramatically, but they can affect the photofraction. The orientations are shown in figure 4.4.

Two plots are shown. A log plot of the response function and a plot with the Compton continuum enlarged. The plots are for crystal shapes 2 and 4. The response functions for crystal 2 for the low energy γ -ray and then for the high energy γ -ray are shown first, followed by those for the large crystal, crystal 4. The log plot is normalized so that the

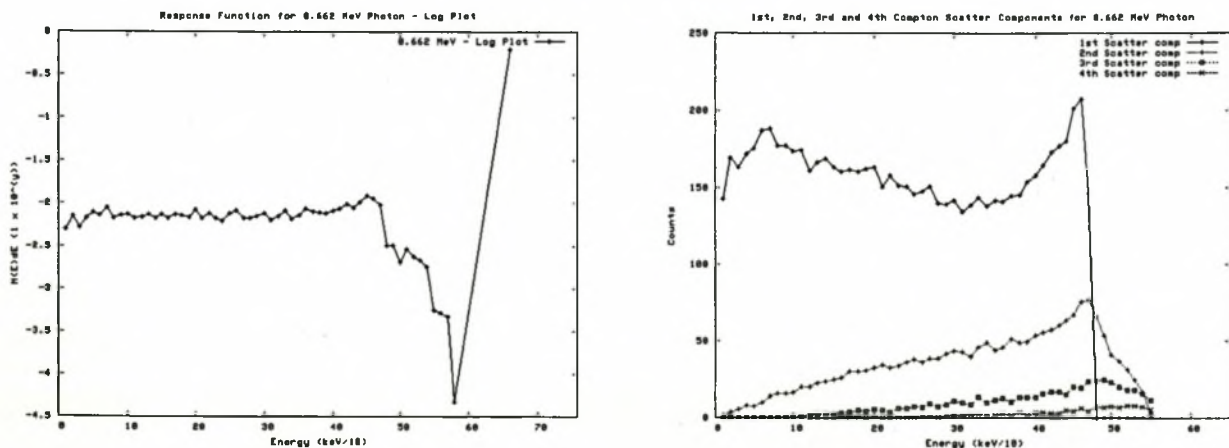


Figure 4.5: Response function and Compton scatter contribution for crystal 2 - 0.662 MeV

response function integrates to unity.

CHAPTER 4. RESULTS AND DISCUSSION

53

In the case of the high energy γ -ray, the response function for crystal 2 is shown in figure 4.6. Once again, the two escape peaks in the high energy DRF emerge.

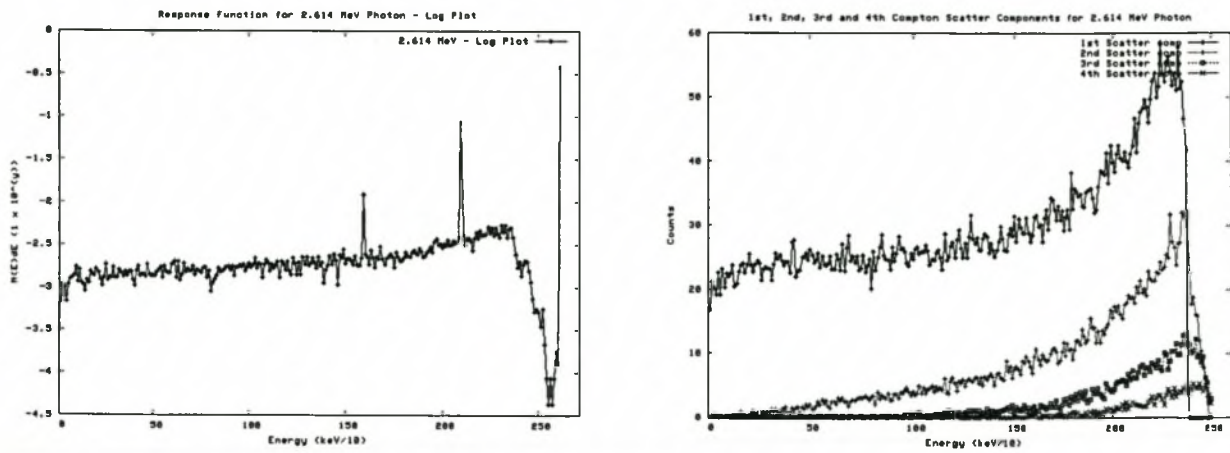


Figure 4.6: Response function and Compton scatter contribution for crystal 2 - 2.614 MeV

For crystal 4, the response functions have a profile, for both the 0.662 MeV and 2.614 MeV γ -rays, similar to that of crystal (2).

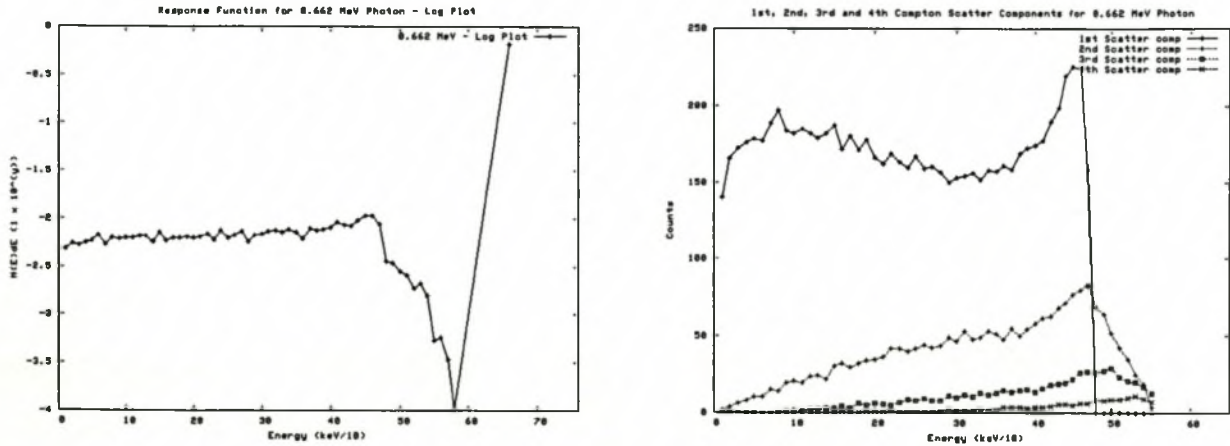


Figure 4.7: Response function and Compton scatter contribution for crystal 4 - 0.662 MeV

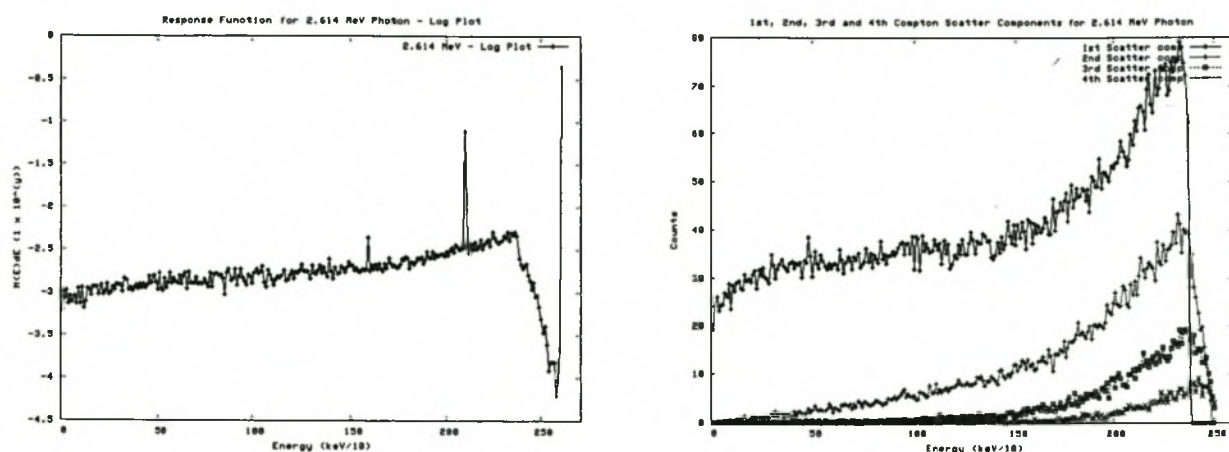


Figure 4.8: Response function and Compton scatter contribution for crystal 2 - 2.614 MeV

Analysis

What is interesting to note is the escape peaks for the 2.614 MeV γ -ray in the case of a small crystal (1) and that of a large crystal (4). From figure 4.9(a) the double escape

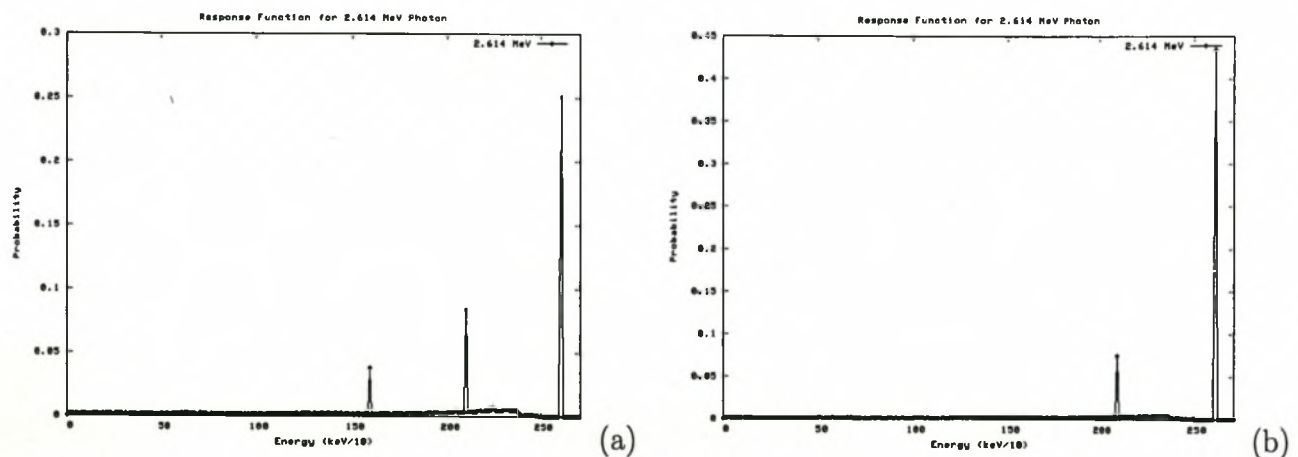


Figure 4.9: Response functions for (a) crystal 1 and (b) crystal 4 - 2.614 MeV

peak is much larger than that in figure 4.9(b). Here, the volume of the crystal affects the numbers of double and single escape events occurring. For the large crystal, the γ -rays produced after electron-positron annihilation are subsequently absorbed by the crystal.

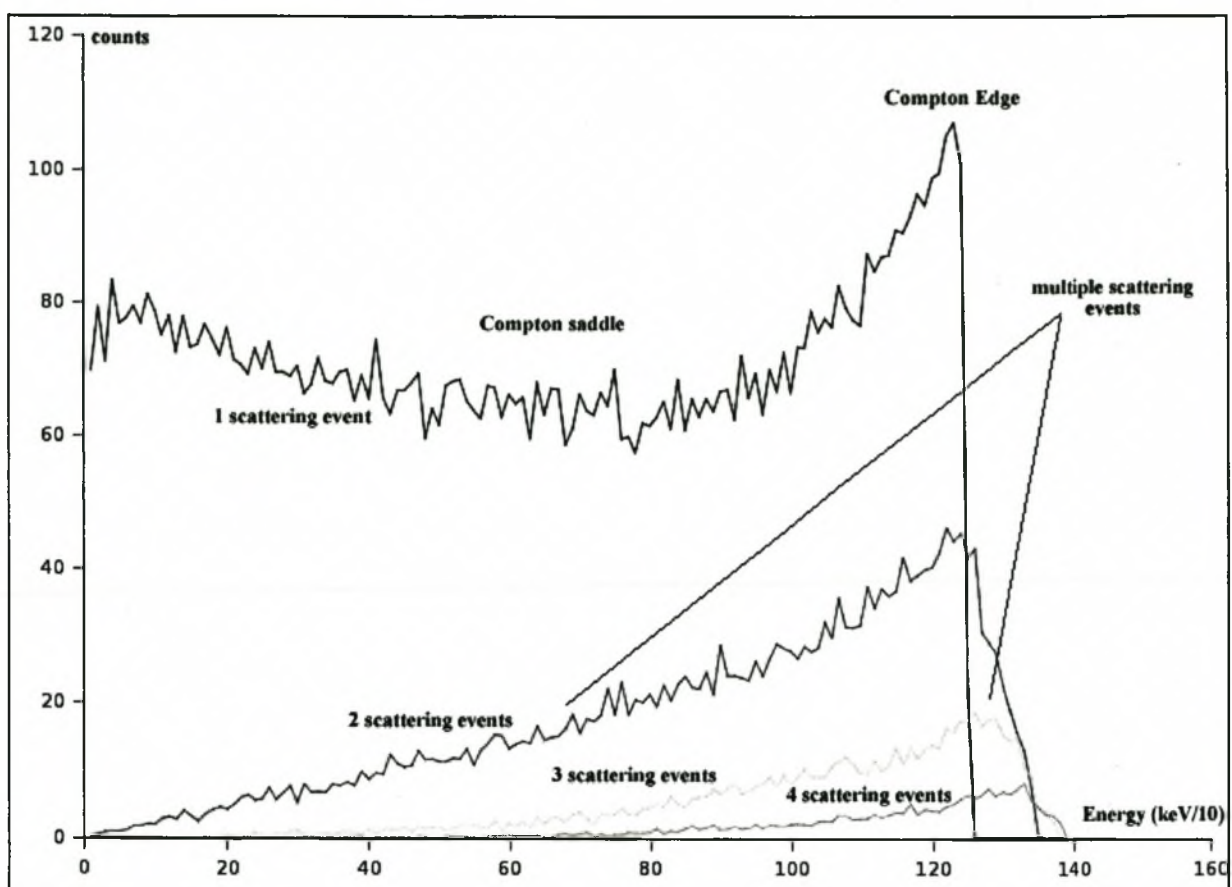


Figure 4.10: Compton scatter contribution

Another interesting feature is the Compton continuum (figure 4.10). For all crystals, the Compton continuum is dominated by the 1st scattering event that takes place. Here the majority of γ -rays transfer energy to the electron in the medium during the first collision. Furthermore, figure 4.10 shows, that the Compton tail is made up of multiple scattering events that occur in the crystal. Here the γ -ray undergoes the primary Compton collision and transfers energy to the electron, followed immediately by a second scattering process transferring another portion of its energy to the second electron. These events occur faster than the spectrometer can respond. The sum of these two energy transfer events is then considered by the spectrometer as a single event. From the Monte Carlo calculation, three and four scattering events do occur successively. The sum of all these scattering events contribute to the Compton continuum.

Another interesting feature of the Compton continuum is the shape of the primary scattering event for the low energy photon compared to that of the high energy photon. Here, few high energy photons will transfer energy to the electron when scattering off an electron at a small angle. High energy photons are more likely to transfer the maximum amount of energy to the electron in a head-on collision (eq. 2.20) when $\theta = \pi$). For both energies, this profile is similar for the two crystals, suggesting that neither the shape of the crystal nor its size influence the energy transfer mechanisms.

4.2 Efficiencies and Photofractions

Efficiencies and photofractions for rectangular crystals with different dimensions were calculated. The input energies used ranged from 0.2 MeV to 2.8 MeV. As mentioned in the previous chapter, all γ -rays simulated begin at the base of the detector in the NIPET code. In terms of efficiencies, the 100000 histories represent the number of γ -rays incident on the detector. The intrinsic efficiency is then the fraction of γ -rays that interact in some manner with the detector material.

NIPET keeps count of those γ -rays that do not interact with the detector. This scenario arises when eq(3.19) is not satisfied. The intrinsic efficiency is then:

$$\varepsilon_{\text{intEff}} = \frac{100000 - \text{noninteracting photons}}{100000} \quad (4.1)$$

For the total efficiency, all counts that recorded an energy deposit in the crystal from zero to the full energy peak were summed. Similarly, the peak efficiency refers to all the counts recorded in the full energy peak. The photofraction is the ratio of the peak and total efficiencies.

4.2.1 Intrinsic Efficiency

NIPET calculates the intrinsic efficiency using eq. 4.1. For a range of energies from 0.4 MeV to 2.6 MeV in 0.2 MeV increments, the intrinsic efficiency is plotted for the crystal

shapes (1), (2) and (4) in figure 4.11. As expected, the intrinsic efficiency increases with the volume of the crystal. The three plots have a sudden change in slope between 1.2 and

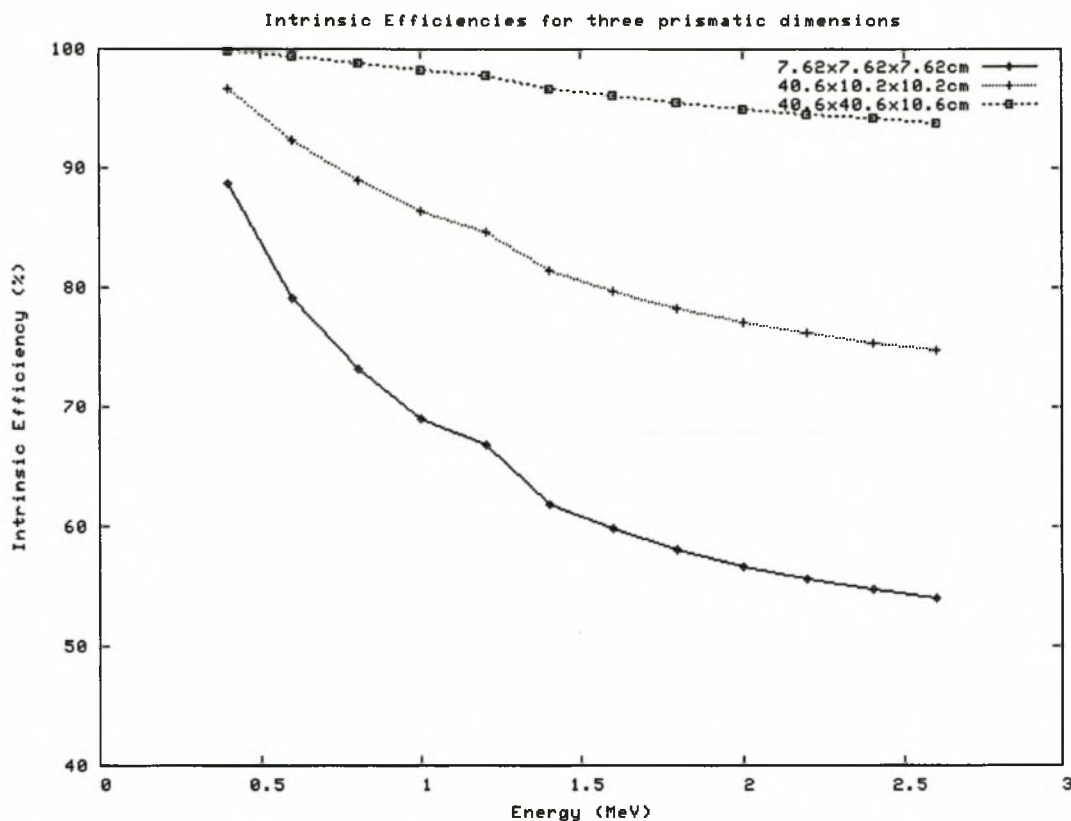


Figure 4.11: Intrinsic efficiencies calculated from eq. 4.1

1.4 MeV. This seems to affect the small crystal more than the larger ones.

Analysis

According to Knoll the intrinsic efficiency is a function of the incident γ -ray energy, the composition of the detector material and the physical thickness of the detector in the direction of the incoming γ -ray [Kno00]. With this in mind, the physical thickness of the detector is the major contributor to the intrinsic efficiency. The use of four $40.6 \times 10.2 \times 10.2$ cm NaI(Tl) detectors indicates that the intrinsic efficiency for the detector system is above 90% across the energy range from 0.2 MeV to 3.0 MeV. This configuration is highly effective when measuring low radioelement concentration in short

Table 4.1: Intrinsic efficiencies in percentage (%) calculated with NIPET

Energy (MeV)	$7.62 \times 7.62 \times 7.62$ cm	$40.6 \times 10.2 \times 10.2$ cm	$40.6 \times 40.6 \times 10.2$ cm
0.4	88.62	96.70	99.88
0.6	79.19	92.36	99.42
0.8	73.21	88.93	98.79
1.0	69.02	86.33	98.20
1.2	66.81	84.69	97.77
1.4	61.94	81.39	96.68
1.6	59.84	79.77	96.08
1.8	58.08	78.28	95.49
2.0	56.65	77.07	94.99
2.2	55.68	76.21	94.55
2.4	54.82	75.42	94.15
2.6	54.01	74.79	93.73

periods of one second.

Portable NaI(Tl) detectors used for in-situ measurements make use of the 3"×3" cylindrical crystal. In the case of a prismatic crystal of similar dimensions, the efficiency for the high energy range (> 2.0 MeV) reduces to around 55%. For low energy γ -rays, the efficiency for the small crystal approaches 80-90%.

Efficiency values given here are questionable, because the method of calculation is admittedly crude. The counts recorded when eq(3.19) is not satisfied, excludes those γ -rays for which the interaction point, calculated with a pathlength that was randomly chosen from a probability distribution, falls outside the active volume. By including these counts as well, better agreement with the literature can be achieved.

However, considering the values for the intrinsic efficiency of a cylindrical 3"×3" NaI(Tl) detector located 30 cm away from a point source given by Capponi *et.al.*, the values agree well with those calculated by NIPET [CMPP83]. Capponi *et.al.* quote a value of 0.771 for a 0.662 MeV photon energy and 0.723 for a 0.835 MeV photon energy as compared to 0.792 and 0.732 respectively calculated by NIPET.

4.2.2 Photofraction

Figure (4.12) is a plot of the photofraction from the three crystals. The program calculates the photofraction using eq. 3.5. As in the case of the intrinsic efficiency, these values are the average of ten simulations for each energy plotted. The energy range from 0.4 MeV to 2.6 MeV in 0.2 MeV intervals produces a consistent profile.

Analysis

The shape of the photofraction curves is almost identical for the three crystal shapes in question. Similar to the intrinsic efficiency profile, the photofraction curves also have a sudden change in slope after 1.2 MeV. This change is more apparent for the smallest

Table 4.2: Photofraction values for three detector dimensions calculated with NIPEL

Energy (MeV)	$7.62 \times 7.62 \times 7.62$ cm	$40.6 \times 10.2 \times 10.2$ cm	$40.6 \times 40.6 \times 10.2$ cm
0.4	0.689	0.729	0.743
0.6	0.566	0.640	0.666
0.8	0.500	0.584	0.620
1.0	0.450	0.545	0.590
1.2	0.446	0.537	0.580
1.4	0.379	0.488	0.538
1.6	0.344	0.463	0.516
1.8	0.308	0.439	0.498
2.0	0.292	0.420	0.478
2.2	0.269	0.398	0.461
2.4	0.267	0.382	0.449
2.6	0.244	0.372	0.437

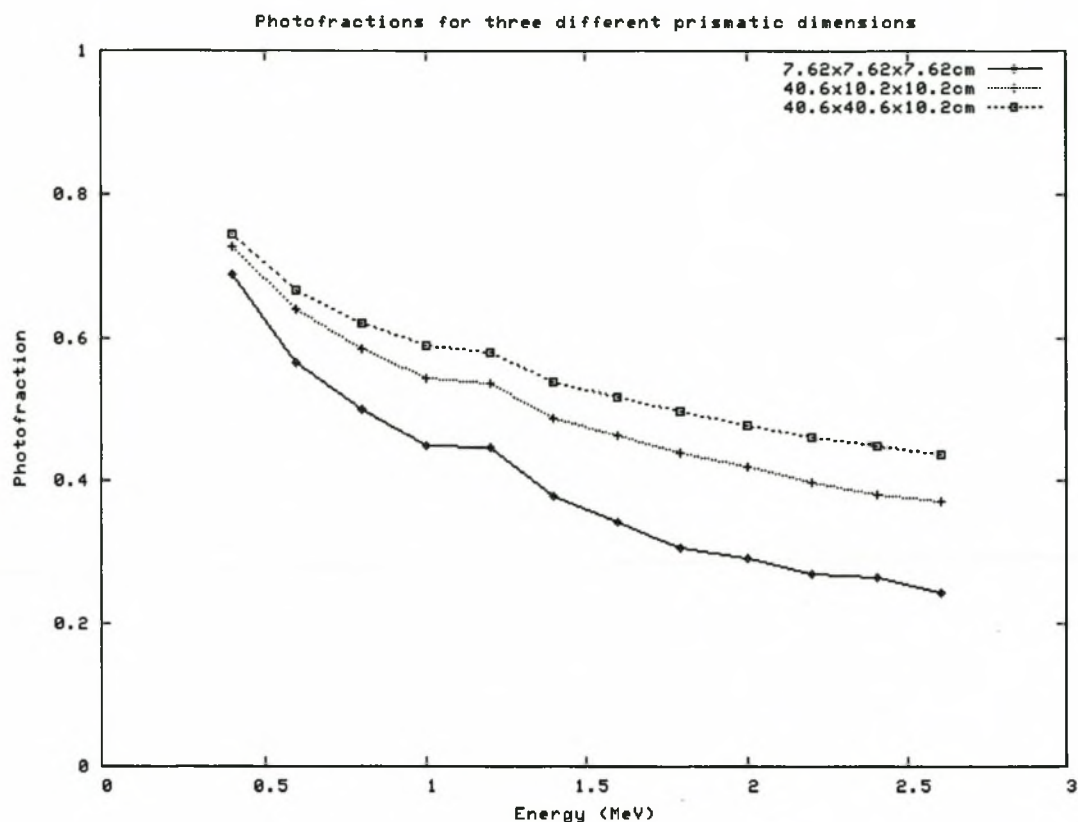


Figure 4.12: Photofraction plot for three crystal shapes

crystal than for the larger ones. Furthermore, in the case of the largest crystal, the magnitude of the slope is significantly reduced.

A similar argument can be formulated for the photofraction as with the efficiency curves that the total interaction cross section is influenced by the contribution of the pair production probability. In addition, the fact that the escape peaks begin to vanish for the larger crystals increases the photofractions for higher energy γ -rays.

The increase in the photofraction for larger crystals can also be ascribed to the *mean free path*, λ in cm, for γ -rays being less than the dimension of the larger crystals. The mean free path is the average distance a γ -ray travels in a medium before an interaction occurs and is given by:

$$\lambda = \frac{1}{\mu_t} \quad (4.2)$$

where μ_t is the total interaction coefficient. In the case of NaI(Tl), λ is 3.5 cm for a 0.662

MeV γ -ray with $\mu = 0.2814 \text{ cm}^{-1}$. For a 2.614 MeV γ -ray, λ is 7.1 cm with $\mu = 0.14 \text{ cm}^{-1}$. The larger crystals can comfortably accommodate this average pathlength associated with the high energy γ -rays in the thorium spectrum.

4.3 Discussion

An infinitely large crystal will have an intrinsic efficiency of 100% and a photofraction of 1.0. Certainly, results generated by NIPET indicate that the intrinsic efficiency increases with an increase in detector crystal volume. The same holds for the photofraction. However, in the case of the latter, the photofraction for high energy γ -rays is influenced by the mean free path and the complete absorption of γ -rays that undergo pair production.

In the event of pair production, the electron-positron pair created lose their kinetic energy within the crystal. When the positron's kinetic energy approaches zero, it can undergo a collision with a free electron and subsequently generate the annihilation γ -rays. Figure 4.9(a) shows that for small crystals, these annihilation γ -rays are more likely to escape the active detector volume, whereas in the case of larger crystals, these γ -rays are more likely to be absorbed. This can be seen by the increase in the double escape and single escape peaks in the detector response function of a small crystal. This points to the fact that in this case as well, the mean free path of the annihilation γ -ray, which is $\lambda = 2.9 \text{ cm}$, is far less than the dimensions of large crystals. Provided that the photon pair was created in the vicinity of the center of the crystal, smaller crystals can absorb these γ -rays. This requirement becomes smaller in the case of larger detectors.

With regards to the photofraction of a NaI(Tl) crystal, the formula presented by Cesana and Terrani (eq. 3.4) was used to verify the photofraction values calculated by NIPET (Table 4.3). There is good agreement between the formula and the simulations. Also, NIPET does not initiate a photon from a source distribution located a distance away from the detector, but from the base of the detector. The agreement between the result of the simulation and the formula provides support for their argument that the

Table 4.3: Photofraction values calculated with eq. 3.4 and from Monte Carlo simulation

Energy (MeV)	NIPET	Cesana & Terrani	Berger & Seltzer	Belluscio <i>et. al.</i>
0.352	0.72	0.76	0.83	0.83
0.609	0.56	0.54	0.63	N/A
0.662	0.54	0.53	0.58	0.57
0.953	0.45	0.43	0.50	N/A
1.120	0.44	0.37	0.45	0.42
1.461	0.37	0.34	0.37	0.36
1.764	0.34	0.27	0.33	0.28
2.614	0.24	0.22	0.20	0.24

photofraction does not depend on the source distribution nor on the source to detector distance.

Table 4.3 shows that there is also agreement with the values published by Berger and Seltzer and Belluscio *et. al.* [BS72, BDLPV74]. Additionally, the photofraction values are not influenced dramatically by the geometry of the crystal. This agreement between calculated values and the literature gives further support for the transport models used in NIPET.

Extending this to larger prismatic crystals, few values are available for comparison. The photofractions for large detectors were compared to those quoted by Billings & Hovgaard and Allyson & Sanderson [AS98, BH99]. In the case of large crystals, there is

Table 4.4: Calculated photofraction values for $16l$ crystals compared with published values

Energy (MeV)	NIPET	Formula	Allyson & Sanderson	Billings & Hovgaard
0.662	0.65	0.84	0.66 (measured)	N/A
1.461	0.53	0.65	N/A	0.64
1.764	0.50	0.54	N/A	0.60
2.614	0.43	0.46	N/A	0.52

disagreement between the values calculated by NIPET and those given in the literature. The calculated value for the 0.662 MeV energy given by Allyson & Sanderson by Monte Carlo simulation is 0.79 which is much higher than that calculated by NIPET which is 0.65. With respect to the values calculated with the formula (eq. 3.4), there is agreement with the photofraction value given by Billings & Hovgaard for the 1.46 MeV γ -ray energy; however this changes for higher energies, where there is better agreement with the values given by this Monte Carlo calculation.

Cesana and Terrani admit that their use of germanium as a reference material is questionable [CT89], but in their defense the formula presented does give, within reasonable limits, good estimates of peak-to-total ratios for small crystal sizes. Although the values for low γ -ray energies are overestimated for large crystals, the formula values approach those calculated with NIPET for higher energies. A follow-on to this study can test the performance of their formula with a different set of interaction coefficients to determine which of its dependencies significantly affects the P/T ratio in the case of large crystals.

Billings and Hovgaard present a geometrical model of an airborne detector crystal. In their case, they assumed the photofraction values as given in table (4.4). They did not explicitly calculate the photofraction. Their Monte Carlo calculations, however, confirm the quoted photofraction values. These authors, however, also state that the values they quoted "would be slightly higher than the real values" [BH99]. By how much higher is not suggested. NIPET's values are within 15% of those of Billings and Hovgaard.

Another noticeable feature of the response function to low and high energy γ -rays, is the Compton continuum. Figure 4.10 shows that the continuum is made up of single and multiple scattering events. Single and double scattering events dominate the Compton saddle. This feature also occurs in germanium detectors as highlighted by Sood & Gardner (2004) [SG04]. Also, the shape of the first Compton scattering component differs for low energy γ -rays and high energy γ -rays. Figures 4.8 and 4.9 indicate that low energy transfers from γ -rays to electrons are suppressed more for high energy γ -rays than for lower energy γ -rays. This behavior is also visible in the second Compton scattering component. This tendency is the same for small and large crystals.

This Monte Carlo photon-electron transport code has been shown to produce acceptable results. The DRFs simulated for mono-energetic photons agree with those of other transport codes. Furthermore, intrinsic efficiency and photofraction values calculated with this code are satisfactory. However, NIPET can be improved. Some of these improvements, which are beyond the scope of this work, are the inclusion of bremsstrahlung, surrounding material and source-detector distance, but as a first esti-

mate the results show excellent agreement with those in the literature. Also, the electron transport model used is highly simplified and a better transport model is desirable. A host of more sophisticated electron transport models is suggested in the literature [AS98, BDLPV74, DJT00, KR02, PGV94]. This will certainly better approximate electron kinetic energy deposition in the crystal at the expense of computational efficiency.

4.4 Radiometrics

Results presented in this work have shown the effectiveness of the 16l NaI(Tl) detector pack in terms of intrinsic efficiency and photofraction for measuring nuclides with low activity. For an environmental spectrum, the efficiency and photofraction of this system for 19 energies associated with the natural radionuclides is shown in figure 4.13. The

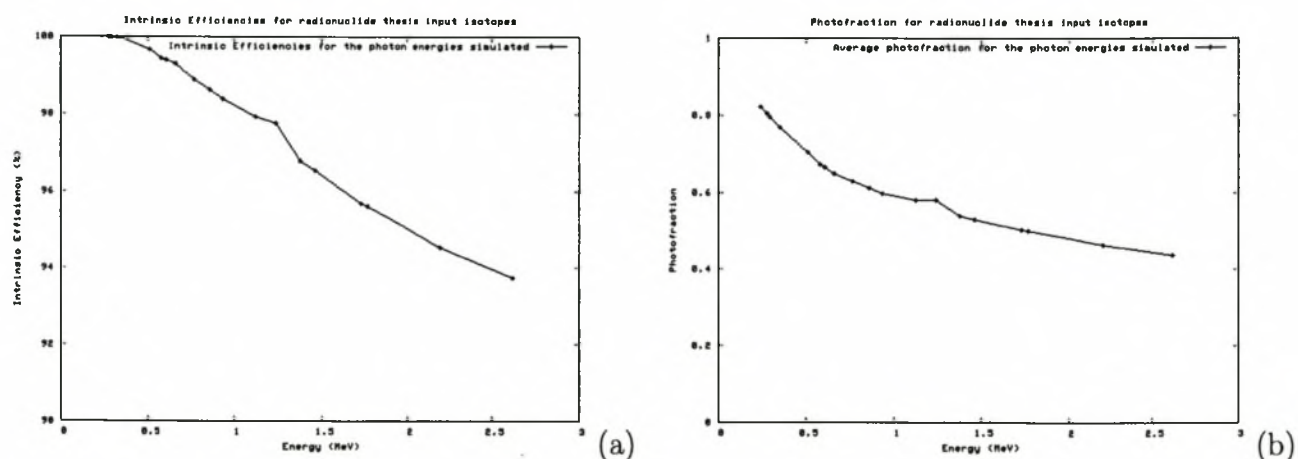


Figure 4.13: Intrinsic efficiency and photofractions for a 16l airborne detector crystal

efficiency is above 90% for the entire energy range. The photofraction is above 40% for high energy γ -rays and approaches 90% for low energy γ -rays.

4.4.1 Airborne Spectrum

GPX, a geophysical airborne survey company in Namibia, graciously provided actual recorded data for this scientific study. Presented below are two plots of the same spectrum.

CHAPTER 4. RESULTS AND DISCUSSION

67

Figure 4.14(a) is the actual measured spectrum and superimposed on this spectrum the resultant spectrum after NASVD processing. Figure 4.14(b) is the same spectrum after it has been corrected as described in section (2.5.3). This processing is the result of expertise and skill on the part of the geophysicists that has a unique artistic attribute.

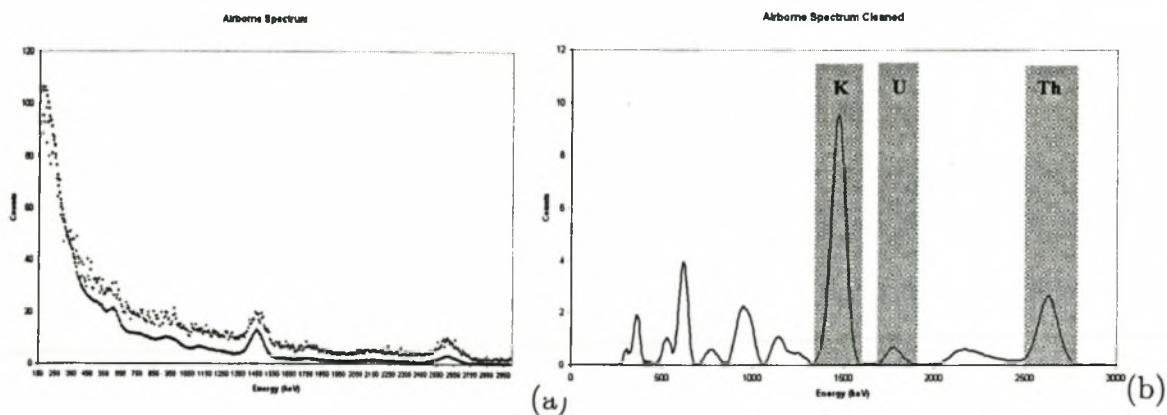


Figure 4.14: Airborne spectrum before processing(a) and after processing (b).

Potassium is windowed between 1.37 to 1.57 MeV, uranium between 1.66 to 1.86 MeV and thorium between 2.41 to 2.81 MeV. The total count window is between 0.4 to 2.81 MeV [IT03]. Both the potassium and uranium windows span 200 keV whereas that for thorium spans 400 keV.

Common to airborne spectra is the high count rate at low energies. This is due to the absorption of bremsstrahlung and backscattered γ -rays from the crystal housing and photomultiplier tubes. This is a clear illustration of the almost 100% efficiency of the detector system at recording low energy pulses. After processing, figure 4.14(b) shows the abundance of low energy spectral information. Multi spectral analysis is becoming important especially in the case of cesium contamination, which is common in the northern hemisphere. Additionally, airborne radiation not originating from terrestrial sources can also be identified. The methods used are briefly mentioned in the following sections.

4.4.2 Radon Contribution

Often during early morning surveying, airborne radon contributes to the measured spectrum. Figure 4.15(a) has a radon contaminated spectrum superimposed on a spectrum without the airborne radiation. Both spectra were measured over the same area spaced 600m apart. The difference is the time of acquisition. The one was measured at 17h00 and the other the following morning at 07h00.

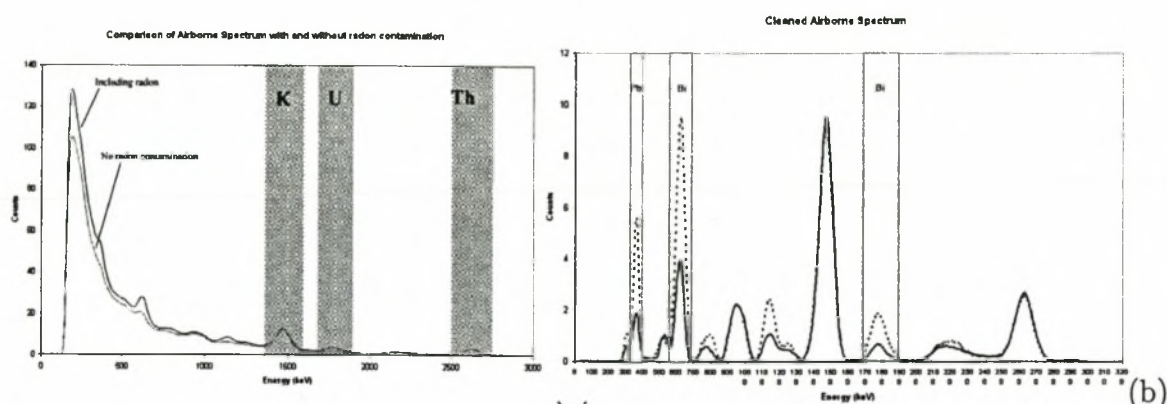


Figure 4.15: Airborne spectra containing airborne radiation compared to 'clean' spectra. From these figures, the accurate measurement of terrestrial uranium is compromised. Airborne radiation in the form of decaying radon into its radioactive daughter products adds a significant contribution of counts to the spectral window of uranium. The removal of this contaminant is difficult, however a few methods are able to achieve this successfully [IT03, Min97, MLB97].

4.4.3 Airborne Radiation Removal Techniques

Several techniques to remove airborne radiation are used by nuclear geophysicists. These methods are: *the spectral-ratio method*, *the full-spectrum method* and *the upward-looking detector method* [IT03, Min97]. In the northern hemisphere, the upward-looking detector method proves popular, whereas in the southern hemisphere the other two methods are used. In the former two methods, the 0.609 MeV photopeak of Bi is monitored and

used to calculate the concentration of airborne radon. Due to the high concentration of cesium-137 in the northern hemisphere, the 0.667 MeV photopeak of ^{137}Cs is located too close to the 0.609 MeV photopeak of Bi. The inherent resolution of NaI crystals limits the measurement of these peaks accurately. Due to this limitation, the upward looking detector method is used during surveys.

4.4.4 Extention to Airborne Radiation Identification

Normally, the 0.609 MeV photopeak of ^{214}Bi is used to estimate the contribution of airborne radiation in relation to the high energy 1.764 MeV photopeak. GPX makes use of the spectral ratio technique but use the ^{214}Pb photopeak located at 0.352 MeV instead of the 0.609 MeV photopeak.

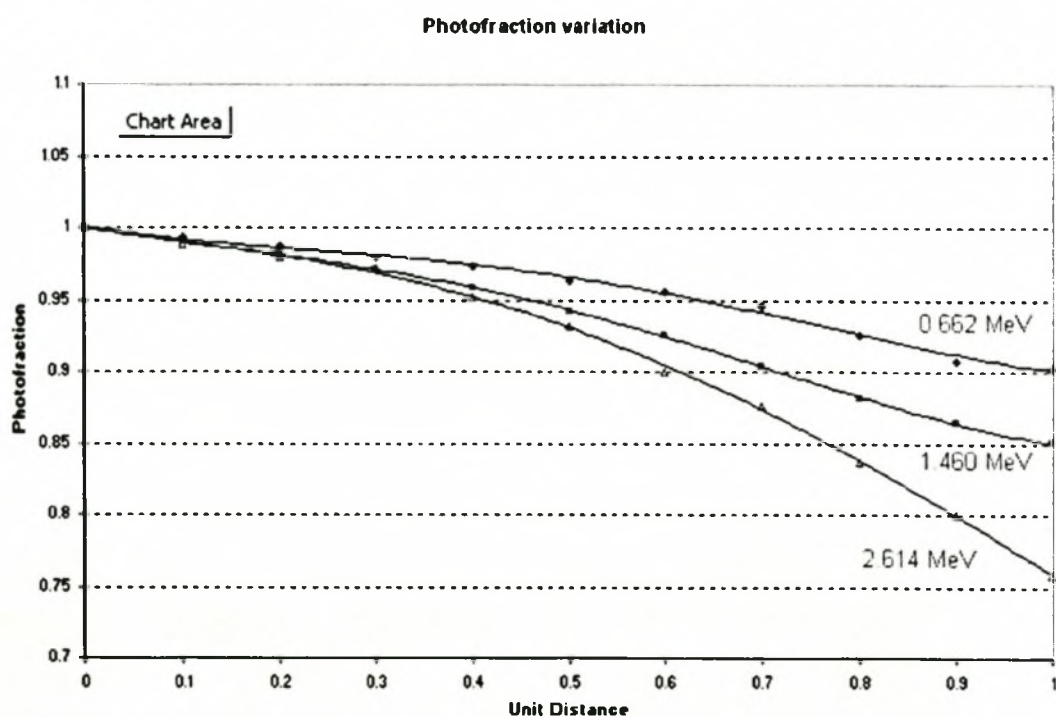


Figure 4.16: Variation of detector photofraction

The low energy lead photopeak has a ten percent higher photofraction than the bismuth photopeak at 0.609 MeV. Furthermore, the resolution of NaI(Tl) is quoted as 7.5%

CHAPTER 4. RESULTS AND DISCUSSION

70

at 0.662 MeV. For the bismuth peak, a certain amount of overlapping will occur between this peak and that of ^{208}Tl during a measurement. These peaks have emission probabilities of 0.46 in the case of bismuth and 0.86 in the case of thallium. Contrary to this, the lead photopeak does not experience this problem because the closest photopeak is the 295 keV peak of ^{214}Pb with an emission probability of 0.19. These peaks can be resolved by the NaI(Tl) crystal. Based on these arguments, their use of this peak to estimate the radon contribution is justified. However, the high background, backscatter radiation and bremsstrahlung contributing to this zone of the spectrum make it difficult to isolate the peak, particularly in the event of low airborne concentration.

Another result worth mentioning is the response of the crystal to radiation incident at the centre of the crystal to that incident through the edge (see figure 4.16). The variation in photofraction was studied by considering the case when a pencil beam of γ -rays strikes the base of crystal. The beam was moved from the center to the outer corner of the crystal in a radial direction. In airborne surveys, this represents the behavior of the crystal to photon absorption depending on where the photons strike the base of the crystal.

For low energy γ -rays, the photofraction drops by almost 10%, whereas in the case of high energy γ -rays the photofraction decreases by as much as 25%. Considering that an airborne detector is surrounded by aluminium and other materials, the 25% of 2.614 MeV γ -rays not absorbed by the crystal are subsequently backscattered off the surround material. Also, electron leakage close to the edge of the crystal can become significant in the event of numerous pair production events. There can also be a possible γ -ray and charged particle source contribution to the exponential increase of the background towards the low energy channels in airborne spectra.

CHAPTER 4. RESULTS AND DISCUSSION

71

Table 4.5: Photofraction values of a 16l NaI(Tl) crystal calculated with NIPET for 13 energies

Energy (MeV)	Photofraction
0.2774	0.805
0.2952	0.796
0.3519	0.768
0.5831	0.670
0.6093	0.664
0.662	0.647
0.8604	0.610
0.9341	0.596
1.1203	0.579
1.461	0.529
1.7645	0.499
2.2041	0.464
2.6146	0.436

Chapter 5

Conclusion

Monte Carlo simulation is a powerful tool when the equipment or conditions are not favourable to perform an experiment. This method of simulation was applied in this thesis. For the purposes of airborne gamma-ray spectrometry, the response of large 16*l* NaI(Tl) detector crystals to mono-energetic γ -rays was studied.

A Monte Carlo based computer program called NIPET was written to simulate the transport of γ -rays and electrons in a rectangular NaI(Tl) crystal. The aim of this exercise is to reproduce the detector response function for a mono-energetic γ -ray source and explicitly calculate the photofraction of these large crystals. The code performed quite well in this respect and showed good agreement with another photon-electron transport code. With this result, the investigation was extended to consider large prismatic crystals.

Unlike other codes that start a γ -ray from a source distribution located a distance d from the crystal, NIPET initiates the γ -ray from the base of the crystal. With this approach, theoretical intrinsic efficiency calculations can be made. NIPET calculates the intrinsic efficiency with the aid of a counter that keeps track of those γ -rays that undergo no interaction in the crystal. Intrinsic efficiency values calculated in this way were found to be over-estimated, even though some agreement does exist with values in the literature. In future assessments of this code, this calculation can be revisited by considering sources located some distance away from the rectangular crystal.

With respect to photofraction values, NIPET showed good agreement with values published in the literature for small detector crystals. This study finds that the shape of the crystal does not alter dramatically the photofraction values for γ -ray energies between

0.2 MeV and 3.0 MeV. For larger crystals the values that are available for comparison disagreed substantially with those calculated with NIPET. However, this work certainly presents explicitly calculated photofraction values for comparison. Experimental data will either support or disprove the photofraction values calculated.

Future refinements, which are beyond the scope of this work, will include the introduction of bremsstrahlung and the effects of the surrounding material. The introduction of other materials or compounds is not a trivial issue and will require careful modelling. However, this addition will give a more realistic approach to airborne detectors. For NIPET, though, this first theoretical study of airborne detectors is reasonable, considering the simplicity of the photon and electron transport model used.

Appendix A

Derivations of Equations

A.1 Derivation of Compton Scattered Photon Energy

Referring to figure (2.5): The momentum of the incident photon is:

$$p = \frac{h\nu}{c} \text{ and after scattering } p' = \frac{h\nu'}{c} \quad (\text{A.1})$$

Conservation of momentum requires that after the collision in the direction of incident photon (x -direction):

$$p = p' \cos \theta + p_e \cos \varphi \quad (\text{A.2})$$

$$h\nu = h\nu' \cos \theta + p_e c \cos \varphi \quad (\text{A.3})$$

where p_e is the momentum of the scattered electron in figure (2.5); and for the y -direction:

$$h\nu' \sin \theta = pc \sin \varphi \quad (\text{A.4})$$

But the relativistic momentum-energy relationship for the electron is:

$$(pc)^2 = T^2 + 2Tm_0c^2 \quad (\text{A.5})$$

$$\Rightarrow pc = \sqrt{T(T + 2m_0c^2)} \quad (\text{A.6})$$

where m_0 is the electron's rest mass and

$$T = h\nu - h\nu'. \quad (\text{A.7})$$

From these equations the relationship between the incident and scattered photon energies can be derived (eq.2.21).

APPENDIX A. DERIVATIONS OF EQUATIONS

75

A.2 The Differential Cross Section

The differential cross section per atom is given by the Klein-Nishina formula as:

$$\frac{d\sigma}{dE} = \frac{\pi r_e^2}{mc^2} \cdot \frac{Z}{\alpha^2} \cdot \left[\eta + \frac{1}{\eta} - \frac{2}{\alpha} \left(\frac{1-\eta}{\eta} \right) + \frac{1}{\alpha^2} \left(\frac{1-\eta}{\eta} \right)^2 \right] \quad (\text{A.8})$$

with $\eta = E/E_0$ and $\alpha = E_0/(mc^2)$. The above equation can be rewritten as follows:

$$\frac{d\sigma}{d\eta} = \pi r_e^2 \frac{mc^2}{E_0} Z \left[\left(\frac{1}{\eta} + \eta \right) - \frac{2}{\alpha} \left(\frac{1-\eta}{\eta} \right) + \frac{1}{\alpha^2} \left(\frac{1-\eta}{\eta} \right)^2 \right] \quad (\text{A.9})$$

$$\frac{d\sigma}{d\eta} = \pi r_e^2 \frac{mc^2}{E_0} Z \left[\frac{1}{\eta} + \eta \right] \left[1 - \frac{\eta \left(2 \left(\frac{1-\eta}{\alpha\eta} \right) - \left(\frac{1-\eta}{\alpha\eta} \right)^2 \right)}{1 + \eta^2} \right] \quad (\text{A.10})$$

$$\frac{d\sigma}{d\eta} = \pi r_e^2 \frac{mc^2}{E_0} Z \left[\frac{1}{\eta} + \eta \right] \left[1 - \frac{\eta \left(\left(\frac{1-\eta}{\alpha\eta} \right) [2 - \left(\frac{1-\eta}{\alpha\eta} \right)] \right)}{1 + \eta^2} \right] \quad (\text{A.11})$$

Using:

$$\eta = \frac{1}{1 + \alpha(1 - \cos \theta)} \quad (\text{A.12})$$

gives:

$$\frac{1-\eta}{\alpha\eta} = \left[1 - \frac{1}{1 + \alpha(1 - \cos \theta)} \right] \cdot \left[\frac{\alpha}{1 + \alpha(1 - \cos \theta)} \right]^{-1} \quad (\text{A.13})$$

$$\frac{1-\eta}{\alpha\eta} = \left[\frac{\alpha(1 - \cos \theta)}{1 + \alpha(1 - \cos \theta)} \right] \cdot \left[\frac{1 + \alpha(1 - \cos \theta)}{\alpha} \right] = 1 - \cos \theta \quad (\text{A.14})$$

Then (13) becomes:

$$\frac{d\sigma}{d\eta} = \pi r_e^2 \frac{mc^2}{E_0} Z \left[\frac{1}{\eta} + \eta \right] \left[1 - \frac{\eta [(1 - \cos \theta)(1 + \cos \theta)]}{1 + \eta^2} \right] \quad (\text{A.15})$$

$$\frac{d\sigma}{d\eta} = \pi r_e^2 \frac{mc^2}{E_0} Z \left[\frac{1}{\eta} + \eta \right] \left[1 - \frac{\eta \sin^2 \theta}{1 + \eta^2} \right] \quad (\text{A.16})$$

Appendix B

Polynomial coefficients

The following tables where taken directly from Avignone & Jeffreys (1981)

B.1 Photoelectric absorption polynomial coefficients

To compute the photo-electric absorption coefficients for NaI(Tl) in cm^{-1}

Energy (MeV)	a_0	a_1	a_2
0.250	2.18×10^1	-2.19×10^2	2.70×10^2
0.550	1.15×10^0	-4.26×10^0	4.20×10^0
1.250	1.60×10^{-1}	-2.83×10^{-1}	1.38×10^{-1}
3.500	1.95×10^{-2}	-1.20×10^{-2}	2.07×10^{-3}

B.2 Compton scattering polynomial coefficients

To compute the Compton scattering coefficients for NaI(Tl) in cm^{-1}

APPENDIX B. POLYNOMIAL COEFFICIENTS

77

Energy (MeV)	a_0	a_1	a_2	a_3
0.150	6.08×10^{-1}	-1.74×10^0	3.20×10^0	0.0
0.700	5.10×10^{-1}	-7.31×10^{-1}	5.07×10^{-1}	0.0
3.500	3.55×10^{-1}	-2.22×10^{-1}	7.72×10^{-2}	-1.02×10^{-2}

B.3 Pair-production absorption polynomial coefficients

To compute the pair-production coefficients for NaI(Tl) in cm^{-1}

Energy (MeV)	a_0	a_1	a_2
1.022	0.0	0.0	0.0
1.280	-2.15×10^{-4}	2.09×10^{-4}	0.0
3.000	-1.33×10^{-2}	9.07×10^{-3}	1.07×10^{-3}

Bibliography

- [AIJ81] F.T. Avignone III and J.A. Jeffreys. Empirical polynomials for computing gamma-ray interaction cross sections and coefficients in Ge and NaI(Tl). *Nucl. Instr. and Meth.*, 179:159–162, 1981.
- [AKBH99] H.K. Aage, U. Korsbech, K. Bargholz, and J. Hovgaard. A new technique for processing airborne gamma-ray spectrometry data for mapping low level contaminations. *Applied Radiation and Isotopes*, 51:651–662, 1999.
- [AM03] F. Arqueros and G.D. Montesinos. A simple algorithm for the transport of gamma rays in a medium. *Am. J. Phys.*, 71(1):38–45, 2003.
- [AS98] J.D. Allyson and D.C.W. Sanderson. Monte Carlo simulation of environmental airborne gamma-spectrometry. *J. Environ. Radioactivity*, 38(3):259–282, 1998.
- [AS01] J.D. Allyson and D.C.W. Sanderson. Spectral deconvolution and operational use of stripping ratios in airborne radiometrics. *J. Environ. Radioactivity*, 53:351–363, 2001.
- [Att86] Frank H. Attix. *Introduction to Radiological Physics and Radiation Dosimetry*. John Wiley & Sons, Inc., 1986.
- [BDLPV74] M. Belluscio, R. De Leo, A. Pantaleo, and A. Vox. Efficiencies and response functions of NaI(Tl) crystals for gamma rays from thick disk sources. *Nucl. Instr. and Meth.*, 118:553–563, 1974.
- [BH99] S. Billings and J. Hovgaard. Modeling detector response in airborne gamma-ray spectrometry. *Geophysics*, 64(5):1378–1395, 1999.

BIBLIOGRAPHY

79

- [BS72] M.J. Berger and S.M. Seltzer. Response functions for sodium iodide scintillation detectors. *Nucl. Instr. and Meth.*, 104:317–332, 1972.
- [BWGV78] G.B. Beam, L. Wielopolski, R.P. Gardner, and K. Verghese. Monte Carlo calculation of efficiencies of right-circular cylindrical NaI detectors for arbitrarily located point sources. *Nucl. Instr. and Meth.*, 154:501–508, 1978.
- [CAS01] A.J. Cresswell, J.D. Allyson, and D.C.W. Sanderson. A code to simulate nuclear reactor inventories and associated gamma-ray spectra. *J. Environ. Radioactivity*, 53:399–409, 2001.
- [CMPP83] M. Capponi, I. Massa, M. Piccinini, and M. Poli. Monte Carlo simulated detector responses to gamma radiations coming from extended sources. *Nucl. Instr. and Meth.*, 217:465–471, 1983.
- [CT89] A. Cesana and M. Terrani. An empirical method for peak-to-total ratio computation of a gamma-ray detector. *Nucl. Instr. and Meth.*, A281:172–175, 1989.
- [DJT00] A. Dubus, A. Jablonski, and S. Tougaard. Evaluation of theoretical models for elastic electron backscattering from surfaces. *Progress in Surface Science*, 63:135–175, 2000.
- [dS01] Jadir C. da Silva. Monte Carlo simulation of nuclear logging detection systems. *Brazilian Journal of Geophysics*, 19(3), 2001.
- [ES02] M.A. El-Sadek. Application of thorium-normalized airborne radio-spectrometric survey data of Wadi Araba area, north-eastern subsurface petroleum accumulations. *Applied Radiation and Isotopes*, 57:121–130, 2002.
- [GS04] R.P. Gardner and A. Sood. A Monte Carlo simulation approach for generating NaI detector response functions (drfs) that accounts for non-linearity and variable flat continua. *Nucl. Instr. and Meth. in Phys. Res., B* 213:87–99, 2004.

BIBLIOGRAPHY

80

- [Hal96] Anthony Hall. *Igneous Petrology*. Prentice Hall, 2nd- edition, 1996.
- [IT03] IAEA-TECDOC-1363. *Guidelines for Radioelement Mapping using Gamma-ray Spectrometry Data*. IAEA, 2003.
- [KMP91] M. Koran, R. Martinčič, and B. Pucelj. In-situ measurements of radioactive fallout deposit. *Nucl. Instr. and Meth. in Phys. Res.*, A300:611–615, 1991.
- [KN78] Kenneth R. Kase and Walter R. Nelson. *Concepts of Radiation Dosimetry*. Pergamon, 1978.
- [Kno00] Glenn F. Knoll. *Radiation Detection and Measurement*. John Wiley & Sons, Inc., 3rd- edition, 2000.
- [KR02] I. Kawrakow and D.W.O. Rogers. The EGSnrc code system: Monte Carlo simulation of electron and photon transport. Technical Report NRCC Report PIRS-701, National Research Council of Canada, 2002.
- [Mai02] M. Maire. GEANT4 tutorial, SLAC, February 2002.
- [Min97] B.R.S. Minty. Fundamentals of airborne gamma-ray spectrometry. *Journal of Australian Geology & Geophysics*, 17(2):39–50, 1997.
- [MLB97] B.R.S. Minty, A.P.J. Luyendyk, and R.C. Brodie. Calibration and data processing for airborne gamma-ray spectrometry. *Journal of Australian Geology & Geophysics*, 17(2):51–62, 1997.
- [Muk76] T. Mukoyama. Range of electrons and positrons. *Nucl. Instr. and Meth.*, 134:125–127, 1976.
- [OSLBF00] C. Oliveira, J. Salgado, M. Luisa Botelho, and L.M. Ferreira. Dose determination by Monte Carlo - a useful tool in gamma radiation process. *Radiation Physics and Chemistry*, 57:667–670, 2000.

BIBLIOGRAPHY

81

- [PAP04] A. Perez-Andujar and L. Pibida. Performance of CdTe, HPGe and NaI(Tl) detectors for radioactivity measurements. *Applied Radiation and Isotopes*, 60:41–47, 2004.
- [PAPI03] C.A. Papachristodoulou, P.A. Assimakopoulos, N.E. Patronis, and K.G. Ioannides. Use of HPGe γ -ray spectrometry to assess the isotropic composition of uranium in soils. *J. Environ. Radioactivity*, 64:195–203, 2003.
- [PGV94] D.E. Peplow, R.P. Gardner, and K. Verghese. Sodium iodide detector response functions using simplified Monte Carlo simulation and principle components. *Nucl. Geophys.*, 8(3):243–259, 1994.
- [Pro79] A. Edward Profio. *Radiation Shielding and Dosimetry*. John Wiley & Sons, Inc., 1979.
- [Pro00] Proceedings of the Second International Workshop on EGS. *Evaluation of Response Functions of 16"x16"x4" Large-sized NaI Scintillation Detector for Environmental Gamma-ray Survey*, number 200-20 in KEK Proceedings, August 2000.
- [RBT89] S.S. Raghuvanshi, B.K. Bhaumik, and S.G. Tewari. A direct method for determining the altitude variation of the uranium stripping ratio in airborne gamma-ray surveys. *Geophysics*, 54(10):1350–1353, 1989.
- [SG04] A. Sood and R.P. Gardner. A new Monte Carlo assisted approach to detector response functions. *Nucl. Instr. and Meth. in Phys. Res.*, B 213:100–104, 2004.
- [SRS02] P. Srinivasan, Anand Raman, and D.N. Sharma. Assessment of calibration parameters for aerial gamma spectrometry systems using Monte – Carlo technique. *Environmental Monitoring and Assessment*, 75:73–85, 2002.
- [YcD98] H. Yücel, M.A. Çetiner, and H. Demirel. Use of the 1001 kev peak of ^{234m}Pa daughter of ^{238}U in measurement of uranium concentration by HPGe gamma-ray spectrometry. *Nucl. Instr. and Meth. in Phys. Res.*, A413:74–82, 1998.

BIBLIOGRAPHY

82

- [Zai99] H. Zaidi. Relevance of accurate Monte Carlo modeling in nuclear medical imaging. *Medical Physics*, 26(4):574–608, 1999.